

Electrical Impedance Tomography: Image reconstruction using Machine Learning



Prepared by:
Matteo Kalogirou
Student Number: KLGMAT001

Department of Electrical Engineering
University of Cape Town

Supervised by:
Dr M. S. Tšoeu
DEPARTMENT OF ELECTRICAL ENGINEERING
University of Cape Town

14 October 2019

Submitted to the Department of Electrical Engineering at the University of Cape Town in partial fulfilment
of the academic requirements for a Bachelor of Science degree in Electrical and Computer Engineering

Declaration

1. I know that plagiarism is wrong. Plagiarism is to use another's work and pretending that it is one's own.
2. I have used the IEEE convention for citation and referencing. Each contribution to, and quotation in, this report from the work(s) of other people has been attributed, and has been cited and referenced.
3. This report is my own work.
4. I have not allowed, and will not allow, anyone to copy my work with the intention of passing it off as their own work or part thereof.

Name: Matteo Kalogirou

Student Number: KLGMAT001



Date: 14 October 2019

TERMS OF REFERENCE

This work is completed for the EEE4022S course, in partial fulfilment of the requirements towards a Bachelor of Engineering Sciences Degree in Electrical and Computer Engineering (BSc Eng ECE).

Broadly, this paper investigates the effectiveness of applying a neural network to solve the reconstruction problem of Electrical Impedance Tomography (EIT). Specifically, this paper aims to demonstrate that a network trained on simulated data can be applied to real data measurements obtained from a simple, time-division multiplexed hardware setup.

The deliverables of the project are:

1. A fully functional time-division multiplexed EIT system
2. Software to control, coordinate and measure data from the hardware
3. A neural network, trained on simulated data, capable of reconstructing an EIT image
4. Schematics and source files of all electronics and software developed
5. A report of the project

To arrive at the deliverables, the following goals are defined:

- Provide a literature review of the current standards and methods used in EIT
- Integrate the μ DAQ microcontroller with the existing hardware
- Obtain experimental data from the hardware system and reconstruct an image from the data
- Calibrate the reconstruction process for the hardware system
- Create a realistic model of the hardware system using EIDORS
- Simulate sufficient training data from the model
- Implement several machine learning algorithms to reconstruct an image from the simulated data
- Apply the machine learning algorithms to the experimental data to reconstruct an image
- Analyse the performance of each network

ACKNOWLEDGEMENTS

Thank you to Ezra America for his helpful contribution of ideas, μ DAQ expertise and friendliness.

Thank you to Mr Dominic De Maar for his hospitality in the control lab and for help with obtaining lab equipment necessary for the project.

Thank you to my parents, for affording me the gift of an education.

ABSTRACT

This paper investigates the practical application of a machine learning algorithm trained on simulated data, to solve the Electrical Impedance Tomography inverse problem.

Electrical Impedance Tomography is a non-invasive medical imaging modality using low-frequency electrical currents to estimate the conductivity distribution of a body from a set of voltage measurements made at the boundary.

The standard methods of estimating the conductivity distribution involve an iterative numerical method to solve a non-linear problem. The problem can be linearised by a suitable regularisation but, the problem is severely ill-posed and therefore requires *a priori* information to ensure a unique and feasible solution. However, computational intelligence is shown to be an effective alternative to the non-linear numerical methods and has the advantage of not requiring any simplifying restrictions or boundary conditions to solve the inverse problem. These learned functions require an enormous amount of data to learn from and it is therefore beneficial to synthesise the training data for practical application.

This paper describes the design and implementation of a time division multiplexed, single source EIT hardware system. The design is implemented using an Enhanced Mirrored Howland current source that is multiplexed to 16 electrodes and is accurate to within $\pm 5\%$ over the expected load impedance range. The hardware system implements an adaptation of the adjacent-drive, adjacent-measurement protocol on a 32 electrode system configured as 16 current injecting electrodes interleaved with 16 voltage measuring electrodes. The multiplexing circuit is shown to deteriorate the signal integrity as current is not isolated to the selected channels.

The paper then shows how the Matlab package, EIDORS, is used to model two representations of the physical system (a 16 electrode system and a 32 electrode system) to generate simulated training data. Two machine learning algorithms, an artificial neural network (ANN) and an amalgamation of multiple artificial neural networks (MANN) are trained on the simulated data.

The ANN shows signs of overfitting and can therefore not be considered, whereas the MANN shows excellent reconstruction accuracy and precision. Of all the reconstructions, the MANN trained on the 16 electrode model exhibits the lowest average mean-squared error ($\overline{MSE} = 0.0017$) and the highest average correlation ($\overline{R} = 0.9625$) with the target output signal. The networks are applied to the experimental data but the reconstructions are unintelligible. This is caused by model mismatch and an unsuitable hardware system.

CONTENTS

1	Introduction	1
1.1	Background to the Study	1
1.2	Problem Statement	4
1.2.1	Research Aims	5
1.2.2	Research Objectives and Questions	5
1.3	Scope and Limitations	5
1.4	Research Contributions	6
1.5	Plan of Development	6
1.6	Report Outline	7
2	Literature Review	8
2.1	Related Hardware Implementations	8
2.2	EIT Hardware	10
2.2.1	Current Source Requirements	10
2.2.2	Voltage Measurement	11
2.2.3	Multiplexers	13
2.3	Current Stimulation Pattern	13
2.4	The Forward Problem	15
2.4.1	Finite Element Method	17
2.5	The Inverse Problem	18
2.6	Static and Dynamic Imaging	19
2.7	Machine Learning	20
2.8	Artificial Neural Networks	21
2.9	EIT Reconstruction and Computational Intelligence	24

3 System Design	26
3.1 Needs and Motivation	26
3.2 Specifications	27
3.2.1 Functional Specifications	27
3.2.2 Non-functional Specifications	27
3.3 Hardware Concepts	28
3.3.1 Single-Source System	28
3.3.2 Multiple-Source System	29
3.4 EIDORS Models	30
3.4.1 EIDORS Structures	31
3.4.2 16-Electrode Model (E16)	32
3.4.3 32-Electrode Model (E32)	33
3.5 Machine Learning Algorithm	35
3.5.1 Input Data	37
3.5.2 Output Data	38
3.5.3 Training Data	38
3.6 ANN Parameters	40
3.7 MANN Parameters	40
4 System Testing	40
4.1 Hardware performance	41
4.1.1 Current Source Stability	41
4.1.2 Control Unit	42
4.1.3 Multiplexed outputs	44
4.2 Measured data	45
4.2.1 Measurement Noise	45

4.2.2	EIDORS Reconstruction	48
4.3	Network performance	49
4.3.1	16-Electrode Model	50
4.3.2	32-Electrode Model	53
5	Results	56
5.1	Network Performance - Simulated data	56
5.2	Network Performance - Measured data	58
6	Discussion	59
6.1	Hardware Performance	59
6.2	EIDORS models	60
6.3	Network Performance	61
6.4	Network Transferal	61
7	Recommendations	62
8	Conclusion	63
A	Github Repository	i
B	E32 Model Input Data Format	i

LIST OF FIGURES

1	The basic setup of an EIT system. The subject, a conductive body, is subjected to a series of current injections and voltage measurements via the electrode array. The hardware systems typically feed this information to a computer for image reconstruction and display. The primary subsystems of the device are shown in boxes and arrows indicate the direction of information exchange. N is the number of electrodes in the system.	2
2	The dispersal of electric field lines superimposed over the scalar potential field through an EIT tank, developed in response to an injected current at two electrodes. Arrows indicate the electric field direction and equipotentials are indicated by dotted lines.	3
3	Work breakdown structure for the project of reconstructing an EIT image from experimental results, using computational intelligence trained on simulated data.	7
4	Project timeline and milestones.	8
5	A non-ideal current source driving a load.	11
6	Mismatched contact impedances on electrodes ($R_{E1} \neq R_{E2}$) resulting in amplification of common-mode signals, V_A . A_D and A_C are the amplifier's differential and common mode gains.	12
7	Non-ideal N:1 multiplexer equivalent circuit [12].	13
8	Measurement pattern for a single stimulation.	14
9	Conductive body, Ω , with a smooth boundary $\partial\Omega$, characterised by a known conductivity distribution, σ	16
10	An EIDORS FEM used in the forward problem.	17
11	Representation of a neurone, the fundamental building block of an artificial neural network.	21
12	Artificial neural network with seven neurones at the input layer, two hidden layers of three neurones each, and seven neurones in the output layer (7-3-3-7 ANN). Lines show connections between neurones.	22
13	Single-source EIT hardware system design.	29
14	Multiple-source EIT hardware design.	30

15	Entity relation diagram of the structures used by EIDORS. Some irrelevant structure members have been excluded. E	31
16	Stimulation-measurement pattern for the 16 electrode model.	32
17	Stimulation-measurement pattern for the 32 electrode model.	34
18	The proposed machine learning problem.	35
19	Classic ANN architecture as compared with the multiple ANN architecture proposed to solve the EIT reconstruction problem.	36
20	ML algorithm input data profile for the E16 model.	37
21	ML algorithm output data profile.	38
22	Flow diagram showing the generation of K simulated training examples for a ML algorithm. K is set to 50 000.	39
23	EMHCS simulation.	41
24	Measured sinusoidal current amplitude through a range of load resistances driven by a 1mA EMHCS. The green band represents a precision of 5%, and 5% error bars are applied to the data points.	42
25	UML activity diagram of the control unit program running on the Arduino.	43
26	RMS voltage profile across each of the multiplexer outputs, shown for four active pairs, E_{1-2} , E_{2-3} , E_{3-4} and E_{8-9}	44
27	A full measurement set for the EIT hardware system.	45
28	Statistical analysis of the measured EIT hardware noise.	46
29	EIT system DC offsets.	47
30	Power Spectral Density of the signal noise.	47
31	Signal to noise ratio (SNR) for each channel in the EIT system. The blue line indicates the average SNR = 16.08 dB.	47
32	EIT experimental measurement data	48
33	EIT reconstruction from measured data.	49
34	E16 ANN robustness tests as compared to the GN one step.	51
35	E16 MANN robustness tests as compared to the GN one step.	52

36	E32 ANN robustness tests as compared to the GN one step.	54
37	E32 MANN robustness tests as compared to the GN one step.	55
38	E16 model MANN reconstruction of the experimental measurements for a banana placed in the tank at 6 and 12 o'clock.	59
39	E32 model MANN reconstruction of the experimental measurements for a banana placed in the tank at 6 and 12 o'clock.	60
B.1	ML algorithm input data profile for the E32 model.	i

LIST OF TABLES

1	Comparison of neural networks with 1 and 10 responses. 96-10-1 repre- sents an ANN with 96 input neurones, 10 hidden layer neurones and 1 output neurone. Results taken from [23].	26
2	Current source stability with variations in load at set frequency.	42
3	Truth Table for the control unit outputs. E_{i-j} represents the electrodes i and j connected to the current source through the multiplexing circuit. . .	43
4	MANN performance evaluation	57

1 INTRODUCTION

This report documents work done on the reconstruction of an image using machine learning for Electrical Impedance Tomography (EIT). This Section will provide a brief background of EIT to familiarise the reader with the imaging modality's history, operation and application. This understanding is important to frame the technology's limitations and the subsequent need for computational intelligence. This Section will also outline the goals and challenges faced in the project, as well as introducing a project plan. This defines each task, its deliverables and scheduled time and resource allocations.

1.1 *Background to the Study*

Since its introduction to the world in 1984 [1], the potential medical benefits of EIT have made it a very promising candidate for routine and continuous medical observation [2]. The technology was initially introduced to observe and monitor gastrointestinal and pulmonary processes, particularly in neonates [3] [4].

Unlike other imaging modalities such as CT or PET scans, EIT does not use ionising radiation. The health risks associated with excessive exposure to radiation often cause cellular mutation or death. EIT is harmless for human application and moreover, allows for continuous monitoring [1].

Additionally, the existing tomographical medical imaging modalities such as CT scans and MRIs, both rely on expensive, difficult to operate medical equipment. Conversely, EIT uses relatively simple hardware, which is significantly less expensive to produce and can be made portable.

Unfortunately, despite the potential advantages of adopting the technology, EIT is an extraordinarily complex problem which has not yet been solved to a sufficient standard for industry wide adoption [2]. The technology simply lacks the spatial resolution and clarity that other imaging modalities can provide.

However, the standard for EIT has steadily improved with advancements in electronics and computing power. A growing interest in the field, along with powerful open source tools, such as EIDORS, have further promoted innovation. This increased accessibility has even allowed EIT to permeate into non-medical applications, such as in human computer interfacing [5].

Figure 1 illustrates a high level abstraction of the system components and their functions.

EIT extracts a cross-sectional view of the internal conductivity distribution within an array of electrodes. A precise amount of current is injected into the conductive body through

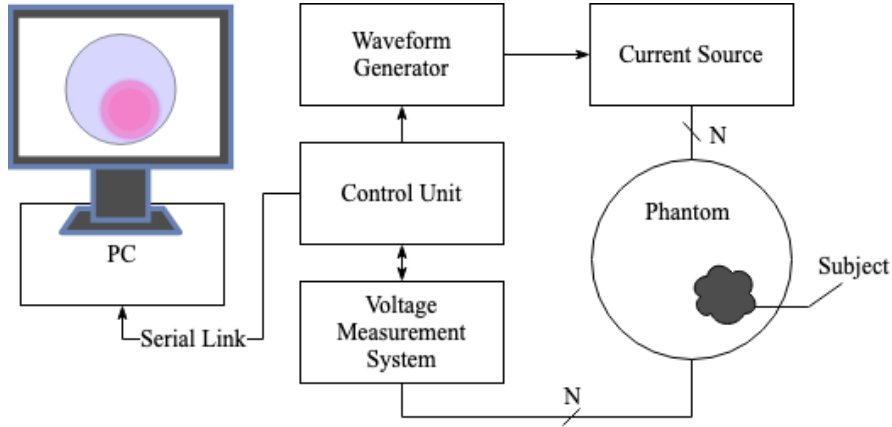
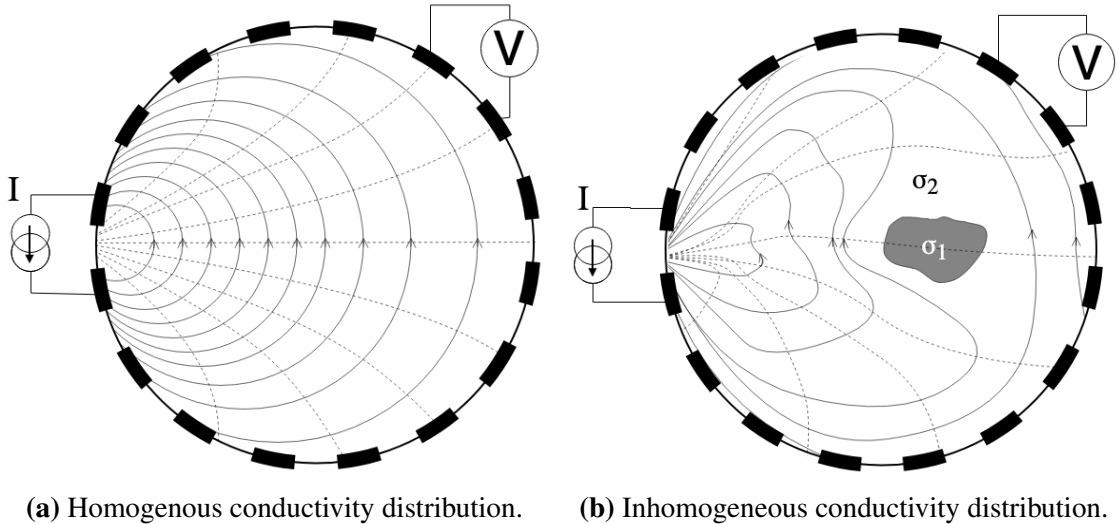


Figure 1: The basic setup of an EIT system. The subject, a conductive body, is subjected to a series of current injections and voltage measurements via the electrode array. The hardware systems typically feed this information to a computer for image reconstruction and display. The primary subsystems of the device are shown in boxes and arrows indicate the direction of information exchange. N is the number of electrodes in the system.

the electrodes placed on the body's boundary. Typically, current is favoured over voltage so that the applied current can be limited to prevent harm in biomedical applications [1]. By measuring the changes in the induced voltage at several positions, an estimate of the internal conductivity can be made. Traditionally, non-linear iterative numerical methods are then required to solve the reconstruction problem and produce a pixel image of the body's internal conductivity map.

Maxwell's electromagnetic equations describe how a change in conductivity can be detected from a series of voltage measurements. Current typically flows from a high to low potential voltage. This potential, $\phi(x)$ may be represented by a group of equipotential lines which lie perpendicular to the electric field.



(a) Homogenous conductivity distribution. (b) Inhomogeneous conductivity distribution.

Figure 2: The dispersal of electric field lines superimposed over the scalar potential field through an EIT tank, developed in response to an injected current at two electrodes. Arrows indicate the electric field direction and equipotentials are indicated by dotted lines.

The electric field \mathbf{E} , a vector field, represents the negative gradient of the potential at a point. This means \mathbf{E} indicates the maximum change in ϕ , along which one expects current to flow. The amount of current flux per unit area is denoted, \mathbf{J} .

These two concepts are related using the idea of conductivity σ , where $\mathbf{J} = \sigma\mathbf{E}$. Conductivity is, therefore, a measure of how well a material conducts electricity. From this simple relationship, we see that current follows the electric fields lines and the electric field are determined by the conductivity distribution.

Therefore, consider some object with conductivity σ_1 in a body of homogenous conductivity σ_2 , where $\sigma_1 \neq \sigma_2$, as in Figure 2b. All current streamlines entering the body will be affected by the change in conductivity, moving the equipotential lines and changing the boundary voltages. In this way, EIT can detect changes in the internal conductivity distribution of a body.

If the internal conductivity distribution is known, then the corresponding boundary voltages can easily be obtained. This is known as the *forward problem* in EIT.

Practically, σ is unknown and must be estimated non-invasively, from the boundary voltages. The process of estimating σ from a set of boundary voltages is known as the *inverse problem*.

Currently, many numerical methods of solving the inverse problem exist [6]. However, all such methods suffer from the ill-posed nature of the inverse problem, requiring a

priori information about the conductivity and boundary conditions to become solvable. Consequently, these methods are prone to a level of uncertainty and are necessarily time-consuming.

Computational intelligence has proven to be an effective modern response to solving the non-linear inverse problem without the need for any prior assumptions. Neural networks have been applied to a wide variety of medical imaging problems since the 1940s with considerable success [2].

The recent rekindling of interest in neural networks has spurred many authors to attempt the *inverse problem* using some form of computational intelligence. Many of these works have shown that machine learning algorithms outperform the classical numerical methods, in terms of improved resolution and signal to noise ratio, see Section 2.9. However, many of these works are restricted to a simulated domain where the networks are never applied to an experimental setup.

Additional research is therefore required to determine the transferability of a machine learning algorithm trained on simulated data, to an experimental setup to solve EIT's inverse problem.

1.2 Problem Statement

Solving the inverse problem is a non-trivial, resource-intensive process which produces low resolution images. Artificial neural networks are a promising alternative to solving the reconstruction process more precisely, but require enormous amounts of data to train. This laborious and time-exhaustive approach of manually gathering data is impractical.

Alternatively, one may create a software model of the physical system and train the network on simulated data. For this network to be transferable to experimental data: the network must be robust to noise, and the model must mimic the exact structure and operation of the system. This includes non-ideal characteristics such as measurement noise and electrode uncertainties.

Furthermore, EIT is fundamentally limited by the hardware configuration. The Caldéron problem says that if we know the complete voltage-current relationship at the boundary, we can determine the conductivity uniquely [1]. However we are limited to 16 distinct measurement positions on the boundary, which produce a maximum of $(16 \times (16 - 1))/2 = 120$ independent measurements [6].

Furthermore, as per the ill-posed nature of the inverse problem: for any given measurement precision there will be some arbitrary conductivity change that is imperceptible to measurements. This imposes a theoretical maximum resolution obtainable from a mea-

surement system.

1.2.1 Research Aims

This paper attempts to demonstrate that a machine-learning algorithm, trained on simulated data, can be used to solve the EIT inverse problem for an experimental system. Secondary goals include accurately modelling the experimental system, and creating a machine learning algorithm capable of solving the inverse problem on simulated data.

1.2.2 Research Objectives and Questions

The main objective of this paper can be summarised as follows:

- Integrate the Eagle DAQ with the existing hardware and successfully reconstruct an image from the system.
- Accurately model the physical system.
- Simulate a large data set for use in training.
- Train several networks using the simulated data.
- Use a network to reconstruct a simulated experiment with a resolution comparable to the Gauss-Newton one-step iterative method.
- Create a network robust enough to reconstruct an intelligible image from the experimental data.

The main research questions that will be asked through the course of this project are, therefore:

- Can the simple time division multiplexed system hardware provide adequate data for the network?
- Is a conductivity change detectable at the boundary?
- How much more robust is a network trained on a realistic model than one trained on ideal data?
- Is it possible to transfer a network directly from simulated data to experimental data?
- Is there a possibility of performing the reconstruction in real time?

1.3 Scope and Limitations

A 12-week period is allocated for this project. This places limitations on the depth of consideration possible for this project. Similarly, a budget of R1500 limits the component

choices for the system design. Since this project aims to be a proof of concept, only the simplest hardware implementation of a 2D EIT system is considered: a 16 electrode, time-division-multiplexed system with an adjacent current injection pattern. This injection pattern is known to have poor spatial resolution furthest from the electrodes by virtue of the configuration.

Furthermore, the networks used in this application can only be as good as the data on which they are trained. The simulated models are sparse FEM with 256 elements to restrict network training times. Therefore, the resulting networks have a limited resolution of 256 finite elements, or output pixels.

This project is not an investigation into the most effective or efficient machine learning algorithms and as such, the algorithms are selectively implemented based on academic recommendation and ease of access. Furthermore, the project will only investigate simple, shallow network structures. No deep networks are considered.

Training the machine learning algorithms through Matlab uses an unspecialised i7 16 GB 3.6 GHz 4 core PC. This limits the number of networks trainable and the complexity of a proposed network structure. A cloud-based TPU, accessed through Google's Colaboratory, is also used to train networks.

This project is not an investigation into numerical reconstruction methods of EIT. As such, all of the numerical reconstruction will be performed using the EIDORS package in Matlab.

1.4 Research Contributions

The significance of this project lies in the potential to validate the transferability of a machine-learning model to a physical hardware system without the need to generate any experimental data. Since machine learning algorithms are capable of reconstructing higher quality EIT images than classical methods, the overall performance of EIT systems may be improved.

Improvements in image resolution may encourage the use of EIT in general healthcare practice, providing a biologically harmless tomographic substitute for routine observation and continuous monitoring applications. With that, the portability and cost-effectiveness of such a device makes medical tomography increasingly economically accessible.

1.5 Plan of Development

The tasks and tools required for completion of the project are shown in the Figure below.

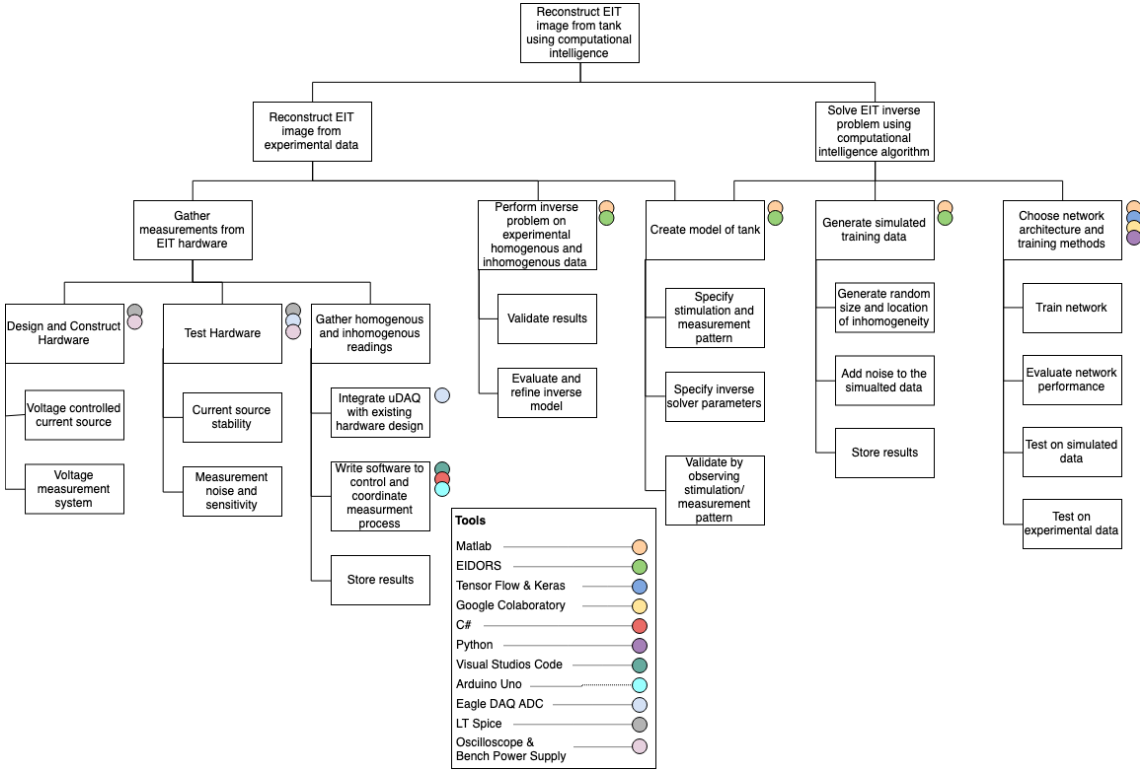


Figure 3: Work breakdown structure for the project of reconstructing an EIT image from experimental results, using computational intelligence trained on simulated data.

The project timeline and estimated task durations are shown in the Gantt chart.

1.6 Report Outline

This paper begins with a literature review in Section 2, which describes the current methods and practices in the field of EIT. The Section also gives a background to the field of machine learning and describes the concepts of training and learning with respect to artificial neural networks. The Section concludes with a review of the current applications of computational intelligence in EIT.

Section 3 outlines the design process undertaken to produce a simple time-division multiplexed EIT hardware system. The modelling process of the system hardware is also described, where two representations of the physical system are created. This Section then describes how the models are used to design and train an artificial neural network to solve the reconstruction problem.

In Section 4, the EIT hardware subsystems are evaluated. The resulting networks are also



Figure 4: Project timeline and milestones.

evaluated on simulated and experimental data. A summary and interpretation of the experimental testing results is then given in Section 5.

Section 6 analyses the underlying causes of the results obtained before providing a number of recommendations to future works in Section 7.

2 LITERATURE REVIEW

Electrical impedance tomography is a multidisciplinary field, only possible through close collaboration of physicists, electrical engineers, computer scientists and mathematicians. This chapter begins by providing a description of the hardware subsystem functions and requirements in an EIT system. The theory involved in the reconstruction process is then addressed before considering machine learning and its application to the reconstruction problem.

2.1 Related Hardware Implementations

The most commonly used EIT hardware configurations are the Sheffield MK1 and MK2 systems, which use the eponymous Sheffield data collection method [1]. These 16-electrode systems are stimulated by a singular sinusoidal frequency of 51 kHz. This stimulation comes from a single voltage-controlled current source that is multiplexed across the electrode array. Each of the 16 adjacent electrode pairs is sequentially driven with 5 mA of

current. The measurement process excludes the driving electrode pair, producing 13 differential voltages for each of the 16 driving pairs. These 208 measurements characterise the system. A phase detector, placed between the 12-bit ADC and the electrodes is used to extract purely resistive signals. The system operates continuously and can produce an image in 79 ms allowing for real-time viewing [4].

The Sheffield protocol is popular for its efficient use of hardware and its simple implementation. However, the efficiency achieved by multiplexing also introduces a major source of error in the form of stray capacitance [1] [4], see Section 2.2.3. This introduces uncertainties on the measurements which drastically reduce the accuracy of the device. A proposed solution lies in increasing the number of surface electrodes to 128, thereby allowing for 8000 independent measurements [4]. However, as the number of electrodes increase, so too does the complexity and expense of such a system. By excluding the imaginary component of the measurements, this system is also incapable of detecting anomalies with reactive impedances.

However, many pieces of literature relating to the construction of relatively simple, low-cost EIT devices are capable of measuring complex conductivities [7] [8].

In [7], Khalighi et al. describe such a device. The authors stress the implementation of a precise hardware system as a means to improve EIT image quality. The 32 electrode system is subdivided into a voltage-controlled current source (VCCS), a multiplexer module, a demodulation circuit, a voltage measurement circuit and the control unit.

The VCCS is a combination of a voltage controlled oscillator, a fourth-order Butterworth band-pass filter and finally a voltage to current converter. This allows the system to produce a nearly pure sinusoidal excitation in the range of 10 to 250 kHz. The voltage to current converter is based on a triple operation amplifier configuration, chosen for its extremely high output impedance(20.2 M Ω to 250.6 k Ω within the operational frequency range).

The singular current source is shared amongst the electrodes by 4, 16:1 analogue multiplexers (ADG506AKN), both sourcing and sinking current on adjacent electrodes. Similarly, 4 multiplexers are used for the measurement system. Notably, no capacitive shielding measures are implemented and the authors mention none of the related issues.

To measure the boundary voltages, this system employs a pulse generator with zero and peak detection of the current signal. This is significant as the resistive and reactive load voltages are expected to be out of phase by 90°. As such, a pulse sample demodulator captures the resistive measurements at current peaks (in-phase) and reactive measurements at zero-crossings (90°phase shift).

The voltage measurements are made on each adjacent pair of electrodes, excluding the

driving pair. Multiplexers route the voltage from each pair to a programmable gain amplifier (AD625) with variable gain to calculate the differential voltages. Due to the precise timing required by the system, an external ADC is employed. The AD1674 has 12-bits of resolution with 1 bit used for polarity. This implies a minimum detectable voltage change of $|2.44| \text{ mV}$. An ATmega128 is used to coordinate the multiplexers, activate the ADC, and communicate the measurements to a PC for remote processing of the data.

The results are then interpreted using the Matlab EIDORS package. The authors compare the system results to two other 16 electrode systems, one of which is a DSP based multifrequency system, and conclude superior reconstruction quality visually [7]. No quantitative comparison is provided, but a battery of tests are conducted to evaluate the quality of reconstructed images under different conditions.

The tests were conducted at 20 kHz with a 1 mA adjacent drive method and included, changing the relative conductivity of the subject within the phantom, varying the number of frames used in the reconstruction, changing the tank shape and investigating the number of electrodes on image quality [7].

Several notable findings arise from these experiments: firstly, the system is more sensitive to changes at the tank centre with fewer electrodes; simply because the larger inter-electrode gaps allow current to diffuse further from the electrodes. Additionally, reconstruction image quality improves greatly with the number of frames taken. This is to be expected as averaging consecutive measurements filters noise from the data.

2.2 *EIT Hardware*

The hardware of the EIT system forms the basis of the device. Although the basic principle of operation remains the same, there are several methods of implementing the system. These different systems are primarily characterised by the number of electrodes, the number of frequencies applied to the body, the number of current sources, the stimulation pattern, and finally the voltage measurement method.

2.2.1 *Current Source Requirements*

In EIT the current source drives the conductive load to generate voltages at the boundary. An ideal current source is characterised by an infinitely large output impedance, Z_O . This allows the current source to reliably deliver a precise amount of current, invariable of the load impedance.

Practically, this is not realisable and represents a common implementation issue. The

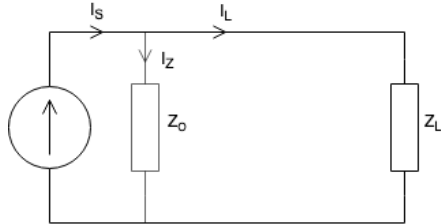


Figure 5: A non-ideal current source driving a load.

significance of this precision allows for boundary conditions to be applied to the *forward problem* (see Section 2.4).

However, since the required Z_O of a device is dependant on the load impedance, Z_L , we can define an achievable Z_O to ensure the current seen at the load, I_L is some acceptable fraction of the source current, I_S .

Assuming a purely resistive load, we can express this relationship as

$$I_S - I_L = \frac{Z_L}{Z_O + Z_L} I_S \quad (1)$$

$$\therefore Z_O = Z_L \left(1 - \frac{I_S}{I_L - I_S} \right) \quad (2)$$

Thus, to ensure that the load sees at least 99% of I_L , $Z_O \geq 99Z_L$, where Z_L is the maximum expected load impedance. It must be noted, in EIT that the load is not guaranteed to be purely real, and the load impedance is a function of frequency, and electrode size [1].

Current sources are also plagued by stray capacitances, which can be modelled as a capacitor in parallel with the current source. At high frequencies, the reactance of the capacitor $X_c = 1/2\pi f$ is small and has the effect of shunting current away from the load. This effectively reduces Z_O .

Naturally, a solution to this stray capacitance involves some form of capacitive cancellation, as described in [1]. Alternatively, one may choose to desensitise the system to complex impedances by only measuring the real component of the signal as in [4] and [9]. However, the trade-off made for simplicity over image quality may only be justifiable for mainly resistive subjects.

2.2.2 Voltage Measurement

The voltage measurement subsystem is responsible for detecting voltages on the electrodes, and discretising the results.

To measure the boundary voltages, one may employ a differential or single-ended approach. Single-ended systems measure the voltage relative to some ground potential whereas differential voltages measure relative to another electrode. In single current-source systems, the differential voltage measurements are preferable for a number of reasons [1].

Firstly, this increases the sensitivity to minute voltage differences at the boundary. To illustrate this, Brown and Seager have shown that in pulmonary imaging, a 100% change in internal resistance may only manifest a 1-10% change in the measured boundary voltage [4].

Secondly, differential measurements typically reduce the dynamic range of measurements, effectively reducing the required ADC precision. The dynamic range is simply the range of the maximum and minimum expected boundary voltages. In an adjacent drive system, the maximum potential is expected when measurements are made nearest to the driving pair and the minimum potential is expected when measurements are made opposite the driving pair. The dynamic range is approximated as 40:1 in [4], implying that a 14-bit ADC can only expect to detect changes of $40/2^{14} \approx 0.244\%$ at the boundary voltage.

However, since the differential measurements are typically made using non-ideal op-amp based devices, they are prone to some common-mode amplification. These errors are accentuated at higher frequencies as the common-mode rejection ratio (CMRR) of an amplifier is usually highest at DC. For high-frequency systems, additional circuitry is required to cancel the common-mode signal through some voltage feedback loop, as used in [10].

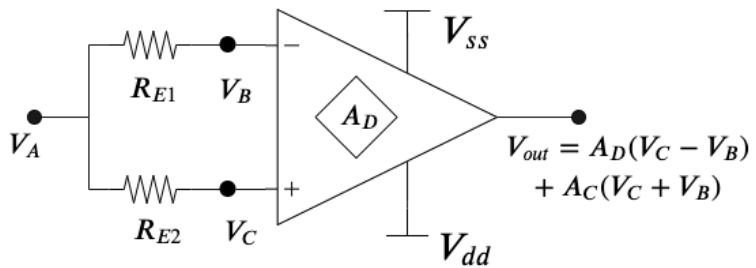


Figure 6: Mismatched contact impedances on electrodes ($R_{E1} \neq R_{E2}$) resulting in amplification of common-mode signals, V_A . A_D and A_C are the amplifier's differential and common mode gains.

Another source of error when measuring differential voltages arises from mismatched contact impedances of electrodes [1]. This effectively accentuates the common-mode error as there is an uneven voltage drop across the electrodes, resulting in a pseudo-

differential signal that is amplified. However, [11] shows that this source of error can be minimised by excluding the imaginary component of the measured signal. Once again, this restricts the reconstructed image to exclude complex conductivities.

2.2.3 Multiplexers

Due to the large number of electrodes required to apply current and measure voltages, it is both impractical and expensive to implement a current source and voltage measurement system for each electrode pair. Instead, a multiplexer is often used to share a common current source or voltage measurement system across each of the electrodes.

There is an inevitable trade-off in the overall performance of the system as the multiplexer introduces many non-ideal characteristics to the circuitry.

Multiplexers have an intrinsic, non-zero resistance which can sully the voltage measurements. Additionally, multiplexers may introduce cross-talk between channels causing unwanted current leakages. However, the most significant non-ideality of a multiplexor lies in the high capacitance seen at the inputs and output of the device [12].

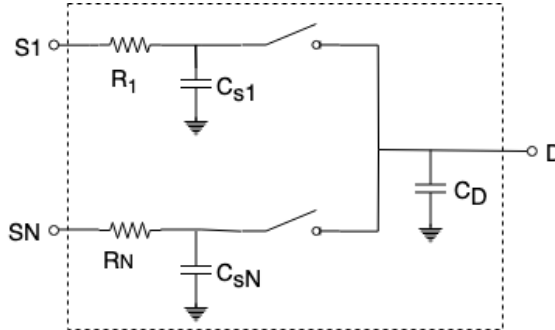


Figure 7: Non-ideal N:1 multiplexer equivalent circuit [12].

From Figure 7, we see that the effective capacitance seen on a conducting channel is $C_s + C_D$ where C_s is the input capacitance and C_D is the output capacitance. This combined with the non-zero on resistance creates a low-pass filter with cut-off frequency $f_c = 1/2\pi R_i(C_{si} + C_D)$.

2.3 Current Stimulation Pattern

The stimulation pattern refers to the selection and orientation of the relative electrode used to apply a current signal to the system. Each stimulation patterns has their advantages

suited to different applications. Figure ?? illustrates two of these patterns applied to a circular electrode array.

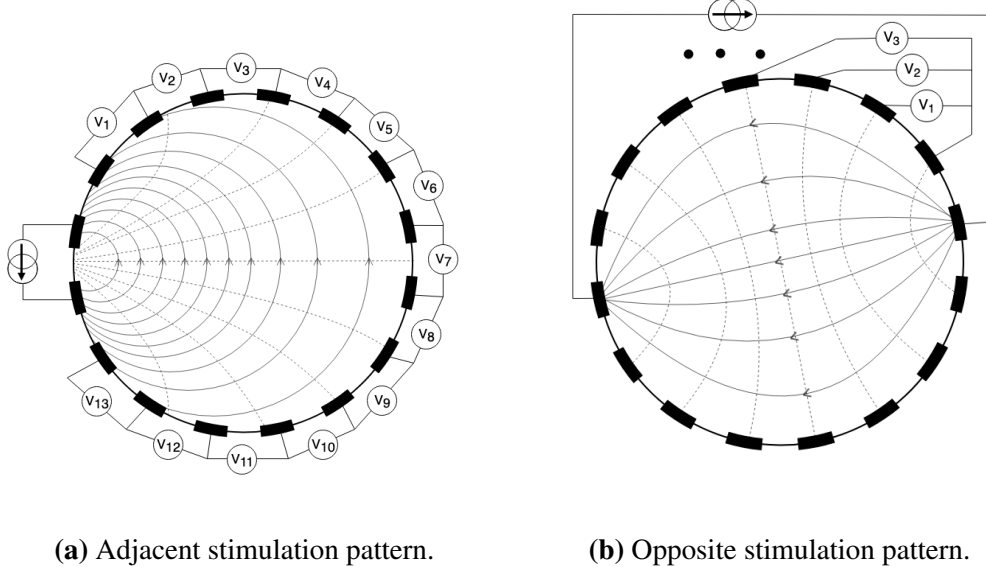


Figure 8: Measurement pattern for a single stimulation.

As the name suggests, the adjacent current stimulation method uses adjacent electrodes to source and sink current. The developed voltages are measured between the electrodes.

To characterise the number of voltage measurements obtained from an L electrode system, note that there are $L - 3$ adjacent differential voltage measurements made for each current injection. This accounts for the exclusion of any differential measurement made on an injecting electrode. Additionally, there are L pairs of adjacent electrodes which result in $L(L - 3)$ differential voltage measurements. The symmetric orientation of electrodes means that only half of the measurements are independent, $L(L - 3)/2$ [13]. Although it is common to exclude the drive-pair, some systems are capable of measuring on all electrode pairs, producing a maximum of $L(L - 1)/2$ independent measurements.

The adjacent injection pattern is characterised by having a high current density near the active electrodes but decreases rapidly as a function of distance from the active pair. This allows for maximal sensitivity near the periphery with poor sensitivity in the centre of the electrode array [13]. This configuration is very susceptible to measurement error due to inaccurate electrode positioning and irregular boundary shapes. This issue is mentioned in [4] and practically demonstrated in [8].

The opposite injection pattern recruits electrodes placed directly opposite one another as injection pairs. This allows for an improved current density uniformity through the

conductive medium, maximising the dispersion of sensitivity. Opposite pairs are therefore best suited to applications such as brain imaging [13].

An electrode nearest to the current source electrode is selected as the reference electrode for differential measurements. Applying the same logic as in the adjacent method, the number of measurements made can be characterised as $L(L - 3)$. However, unlike in the adjacent method, there are only $L/2$ opposite electrode pairs to apply measurements to and therefore the number of independent measurements is reduced to $L(L - 3)/4$, significantly fewer than the adjacent method [13].

2.4 The Forward Problem

Recall that the aim of the *forward problem* is to recover the boundary voltages developed over a given conductivity distribution in response to a known stimulation.

To do so, we first define the electric field \mathbf{E} and current density \mathbf{J} according to Maxwell's equations:

$$\nabla \times \mathbf{E} = -\frac{\partial \mathbf{B}}{\partial t} \quad (3)$$

$$\nabla \times \mathbf{H} = \varepsilon \frac{\partial \mathbf{E}}{\partial t} + \mathbf{J} \quad (4)$$

Where the magnetic field \mathbf{H} , is linearly related to the magnetic flux \mathbf{B} , through the permeability μ and ε represents the permittivity. Practically, this implies that a current density \mathbf{J} induces a rotating magnetic field \mathbf{H} and this change in \mathbf{H} will cause the electric field to rotate. The time varying electric and magnetic fields can be re-expressed in phaser form, $\mathbf{E}(x, y, z; t) \rightarrow \text{Re}\{\mathbf{E}(x, y, z)e^{j\omega t}\}$, the time harmonic equations are then,

$$\nabla \times \mathbf{E} = -j\omega\mu\mathbf{H} \quad (5)$$

$$\nabla \times \mathbf{H} = \mathbf{J} + j\omega\varepsilon\mathbf{E} \quad (6)$$

Ohm's law in continuum states that the conductive current density \mathbf{J}_c is a function of the conductivity σ and the electric field \mathbf{E} . The total current density $\mathbf{J} = \mathbf{J}_c + \mathbf{J}_s$, is a combination of the conductive and source currents. However, in low-frequency applications \mathbf{J}_s is negligible [1], such that

$$\mathbf{J} \approx \mathbf{J}_c = \sigma\mathbf{E} \quad (7)$$

Combining Equations 6 and 7 gives

$$\nabla \times \mathbf{H} = (\sigma + j\omega\varepsilon)\mathbf{E} \quad (8)$$

Notably, for the purposes of EIT, it is assumed that $\omega\mu\mathbf{H}$ is negligible, resulting in no rotation of the electric field $\nabla \times \mathbf{E} = 0$. Therefore the scalar potential $\phi(x, y, z)$ can be described in terms of \mathbf{E} as

$$\mathbf{E} = -\nabla\phi(x, y, z) \quad (9)$$

Recall that some \mathbf{J} is applied at the boundary $\partial\Omega$. Since there are no internal current sources, Kirchhoff's current law in continuum states that the net current flux about $\partial\Omega$ must be zero, so $\nabla \cdot \mathbf{J} = 0$. Therefore, taking the divergence of both sides of Equation 8 and substituting Equation 9 into the result gives

$$\nabla \cdot (\sigma\nabla\phi) = 0 \quad (10)$$

Which produces in a second order, partial differential equation where $\sigma > 0$.

$$\frac{\partial}{\partial x} \left[\sigma \frac{\partial\phi}{\partial x} \right] + \frac{\partial}{\partial y} \left[\sigma \frac{\partial\phi}{\partial y} \right] + \frac{\partial}{\partial z} \left[\sigma \frac{\partial\phi}{\partial z} \right] = 0 \quad (11)$$

To solve for Equation 11 uniquely, a boundary condition must be applied. Two such boundary conditions, Dirichlet and Neumann, are commonly used. The first of which, defines the voltage at the boundary according to some function, f such that

$$\phi|_{\partial\Omega} = f \quad (12)$$

Practically, this is unsuitable to EIT for two reasons. First, it requires that a voltage function is applied across the entire boundary when typically electrodes only cover a portion of the boundary. Secondly, it is preferable to control applied currents for biomedical application.

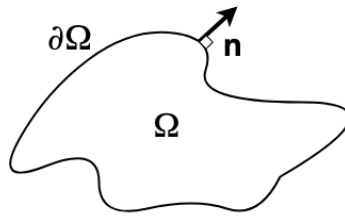


Figure 9: Conductive body, Ω , with a smooth boundary $\partial\Omega$, characterised by a known conductivity distribution, σ .

The Neumann boundary condition imposes restrictions on the current density at the boundary, j . If \mathbf{n} is the outward normal vector at $\partial\Omega$ then

$$\sigma \frac{\partial\phi}{\partial\mathbf{n}} = j \quad (13)$$

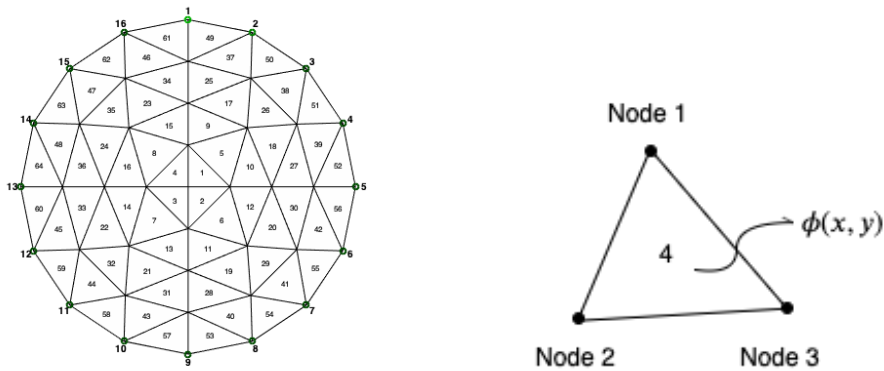
$$\therefore \sigma \nabla\phi \cdot \mathbf{n} = j \quad (14)$$

Any function j may be chosen to satisfy this boundary condition but it must be noted that j is not unique, since $\partial/\partial n(\phi + k) = \partial/\partial n(\phi)$ but $(\phi + k) \neq \phi$. Practically, this means that the voltage reference point is unknown. The Neumann boundary condition is preferable as it accounts for the distinct positioning of electrodes at the boundary, each with a known surface current density.

Although the PDE has been described, the model must first be discretised to solve for the scalar field. This is typically done using a finite element method (FEM), although finite difference methods and boundary element methods may also be applied [14].

2.4.1 Finite Element Method

Finite element methods (FEM) allow us to solve a continuous partial differential equation such as, Equation 11, discretely. This is done by first defining a mesh to discretise the PDE. This mesh subdivides the problem into a finite number of elements, hence the name. In 2D problems, these elements are polyhedra. The method then defines and imposes a basis function onto each element. By specifying the boundary conditions, a solution to each of the elements can be found by solving a set of linear equations. The solution to each element is then defined by a polynomial whose order depends on the number of vertices of the element [14].



(a) Sparse FEM of an EIT circular tank with 16 electrodes and 64 elements.

(b) The fourth element in the mesh. Each triangular element has three nodes which are used to define the potential within the element.

Figure 10: An EIDORS FEM used in the forward problem.

For each element, the potential is a function of spatial position and is represented by a

polynomial in the form:

$$\phi(x, y) = \alpha_1 + \alpha_2 x + \alpha_3 y \quad (15)$$

With α_1 , α_2 and α_3 being scalar parameters defined by the element's geometry. The potential inside the element can also be represented as a function of the node voltages. The FEM solution is expected to converge as the number of elements increases, or as the order of the polynomial increases [14].

In EIT, the FEM allows us to solve for the boundary voltages, $\phi|_{\partial\Omega}$ given σ and a set of boundary conditions, ie Neumann boundary conditions specifying the injected boundary currents. The FEM allows for the PDE to be reformatted into an algebraic form

$$\mathbf{Y}\mathbf{v} = \mathbf{i} \quad (16)$$

Here, \mathbf{Y} represents the admittance, or inverse conductivity, at each node, as described in [15]. The node potentials are represented by the vector \mathbf{v} and the current entering each node is described by \mathbf{i} . At this point, the Neumann boundary conditions are applied and cause the matrix \mathbf{Y} to become sparse. The equation is then solved using specialised matrix algebra.

2.5 The Inverse Problem

The EIT inverse problem aims to solve the conductivity distribution from the measured boundary voltages ϕ_{meas} . This is typically performed using iterative numerical methods such as Gauss-Newton or Tikhonov. A good description of these numerical methods can be found in [15] and [6]. These methods employ a cost function to minimise the error between ϕ_{sim} and ϕ_{meas} [14]. These algorithms can be summarised in the following steps:

1. Estimate a set of conductivities to describe the conductivity distribution, $\{\sigma\}$
2. Perform the forward problem using $\{\sigma\}$ to obtain the simulated boundary voltages, ϕ_{sim}
3. Compare ϕ_{meas} against ϕ_{sim}
4. Adjust $\{\sigma\}$

Steps 2 to 4 are repeated until $\{\sigma\}$ adequately describes ϕ_{meas} , with the solution generally improving as the number of iterations increases [14]. However, the ill-posed nature of the problem means that a solution may not exist, or that a solution is not unique [1].

According to Hadamard, a well-posed model exhibits the following characteristics:

1. For all admissible data, there exists a solution.
2. For an admissible set of data, the solution is unique.

3. The solution depends continuously on the data.

The reconstruction problem in EIT violates all of these conditions. One causal factor being the so-called non-locality of the system. EIT applies relatively low-frequency excitations to the body of interest. As a result, the exciting signal disperses through the medium such that the accumulated interference with the medium cannot be localised to a single path [6]. Therefore, a change in the conductivity in any part of the medium will affect all subsequent measurements [1].

However, a solution can still be obtained if each condition is treated. Firstly, when solving for σ one assumes that there *is* an underlying conductivity distribution, so a solution must exist. Secondly, to treat an unfeasible solution, one may project this solution onto the nearest feasible solution in the solution set [1].

Characteristic 3 is in fact, the most problematic. The perceptible change in conductivity is intrinsically dependent on the measurement quality and type [1]. As there are physical limitations imposed on the hardware, regularisation of the problem becomes a prerequisite to produce a smooth, unique solution set [6].

The Gauss-Newton method iteratively solves the inverse problem using the Newton-Raphson method. The cost function U , is described by [14]

$$U(\{\sigma\}) = \frac{1}{2} \left[\phi_{pred}(\{\sigma\}) - \phi_{meas} \right]^T \left[\phi(\{\sigma\}) - \phi_{meas} \right] \quad (17)$$

To obtain the set $\{\sigma\}$ which minimises $U(\{\sigma\})$, we differentiate Equation 17 with respect to some incremental change in the conductivity, $\Delta\sigma$, set the equation to zero and solve for $\{\sigma\}$. The calculated $\Delta\sigma$ represents the changes in $\{\sigma\}$ which move the solution towards convergence. The updated $\{\sigma\}$ is then used in the next iteration.

2.6 Static and Dynamic Imaging

In EIT there are two methods of obtaining an image, namely static or dynamic imaging. Static imaging implies that the inverse problem is computed solely from a set of boundary voltages. No *a priori* information is required to compute the image making the reconstruction algorithm extremely sensitive to measurement noise and electrode placement uncertainty [9].

Static imaging is preferable for *in vivo* applications. Although, the problem of accurate and precise electrode placement becomes increasingly more difficult when the electrodes are intended to be placed on subjects whose size and shape varies [4].

Dynamic imaging, also called difference imaging, uses *a priori* information in the form

of a reference. Reference measurements are typically obtained from a homogenous distribution of the phantom. The reconstruction algorithm is then applied to the measured difference between the reference and inhomogeneous measurements. In this way, the change in conductivity can be detected. This limitation makes difference imaging more robust to noise, measurement error, electrode contact impedance, and electrode placement uncertainty by virtue of the fact that only the conductivity differences are detected [16]. The common sources of error are cancelled out.

2.7 Machine Learning

Machine learning is a broad term that is generally understood to describe the process of having an algorithm perform some task, and improve its performance of the task through experience [17]. Learning describes the process of improvement.

Machine learning algorithms can be divided into several categories which utilise different representations of a learned function. These include:

- **Supervised Learning.** Here, a target function is defined and presented in conjunction with a training example. The algorithm is then expected to learn some function capable of mapping the input data to the output data. When applied to qualitative data, this learned function is termed a *classification* problem, whereas *regression* is used for quantitative data.
- **Unsupervised Learning.** In this learning function, the algorithm is not presented with a target function and instead seeks to uncover some underlying pattern in the data. These algorithms tend to project data points into higher dimensions to form clusters between similar data points.

Each type of learned function applies to a wide variety of problems, although the data type and desired target usually determine the available methods.

Since the target function is parameterised, we can think of the learning process as searching through a hypothesis space, H , to best describe the observed data. Clearly, as the number of observed training examples increases, the larger H becomes and the greater the chance of encompassing a valid solution.

A well-defined problem is necessary to efficiently navigate the solution space. This means that both the task and performance metric should be well defined. Sufficiency of data will ensure that a reasonable section of H can be explored but the quality of the data will ultimately determine the obtainable accuracy of the trained function.

2.8 Artificial Neural Networks

As the name suggests, artificial neural networks (ANNs) have loosely been derived from biological neural structures found in the brain. The network is composed of many individual units called neurones, or perceptrons. The neurones are arranged in layers of variable sizes with the first and last layers being the input and output layers. The intermediary layers are termed *hidden* layers. Neural connections are formed between layers, with information diffusing through the network from the input layer, this is a *feedforward* network. In this way, ANNs are analogous to directional graphs. Similarly to graphs, ANNs can also be cyclic, exhibiting some form of feedback within the network. These ANNs are called *recurrent* and will not be considered here. We will focus on the acyclic directed ANN structure.

The fundamental building block of the network is the same. Each neurone accepts a number of inputs \vec{x} , applies a weighting to the inputs, \vec{w} , and sums the linear combination of weighted inputs (Figure 11). An additional bias term, w_0 , is included in the summation and is analogous to imposing a threshold [17].

The resulting sum is then subjected to an output function called the *activation* function. As the name suggests, this function in conjunction with w_0 , determine when the neurone is activated. More subtly, the activation function serves to limit the output of each neurone.

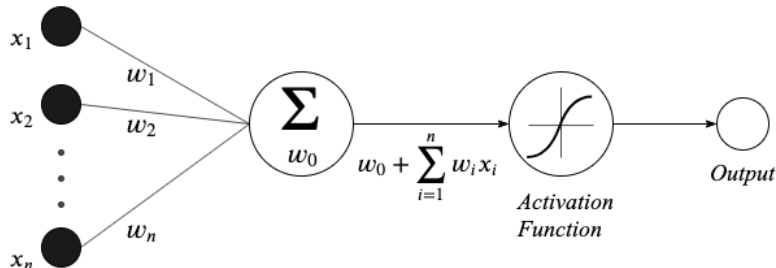


Figure 11: Representation of a neurone, the fundamental building block of an artificial neural network.

Common activation functions include $\tanh \in [-1; 1]$, $\text{sigmoid} \in (0; 1)$, $\text{relu} \in [0; \infty)$ and even linear $\text{purelin} \in \mathbb{Z}$ functions. Let the activation function in Figure 11 be the \tanh function, so that the neurone's output is:

$$o = \tanh \left[w_0 + \sum_{i=1}^n w_i x_i \right] \quad (18)$$

The output, o , is then fed to the subsequent layer in the network. Each neurone has a unique set of weights and need not have the same activation function. Typically, the

outputs of the hidden layer are limited by a squashing function such a *tanh*, and the output layer activation function is determined by the target data type.

ANNs fall under the **supervised** category of algorithms and can be used for both classification and regression problems. In *classification* problems, the number of outputs corresponds to a distinct number of classes, the network therefore assigns a prediction score to each class based on the input. Here $o \in [0; 1]$ which implies *sigmoid* activation. In *regression* problems, the output may not be normalised. Therefore, a linear, or partly linear (*relu*) activation function is required.

The structure of a generic ANN is shown in Figure 12.

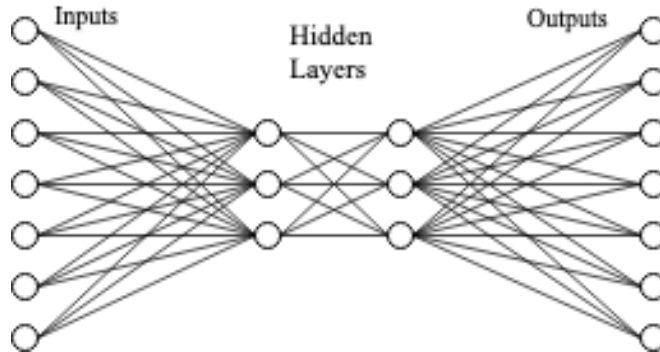


Figure 12: Artificial neural network with seven neurones at the input layer, two hidden layers of three neurones each, and seven neurones in the output layer (7-3-3-7 ANN). Lines show connections between neurones.

Learning, with reference to ANNs, describes the process of tuning the weights and biases of each neurone to minimise the loss between the network output and the target output. To do this we must define the learning algorithm as well as the performance metric.

As in any optimisation problem, we can assign a cost function to search through the hypothesis space H for a set of weights and biases that minimise the error between the target outputs and the network outputs. The process of updating the weights and biases of each neurone is defined by the *Back-propagation* algorithm. Since the training examples only specify a target for the output neurones, the algorithm carries the output error through the preceding layers of neurones to update each set of weights. A neurone's weights are updated according to their impact at the output layer. Hence, back-propagation.

Typically, *back-propagation* quantifies the performance of the network using the mean squared error between target and network outputs. We define the sum of squared errors at the output as [17]:

$$E(\mathbf{w}) = \frac{1}{2} \sum_{d \in D} \sum_{k \in N} (t_{kd} - o_{kd})^2 \quad (19)$$

Where \mathbf{w} is a vector of weights for each output neurone, d is a training example in the set D and k is one of the output neurones for a network with N outputs.

By taking the negative gradient of the error, E with respect to the weights we can define the steepest path along the hyperplane to reduce E . The activation function must, therefore, be differentiable. We navigate through the hyperplane by adjusting \mathbf{w} according to some fraction of $-\nabla E$ called the learning rate. Note that this method can only guarantee convergence on a local minima. Equation 20 defines the weight update rule.

$$\mathbf{w} \leftarrow \mathbf{w} + \Delta \mathbf{w} \quad (20)$$

Where $\Delta \mathbf{w} = \eta \frac{\partial E}{\partial \mathbf{w}}$, and η is the learning rate.

Algorithm 1: Back-propagation using stochastic gradient descent

Data: Training examples D , learning rate η , number of input nodes n_{in} , number of layers m , number of output nodes n_{out}

Result: Trained ANN

Create ANN with defined shape;

Randomly initialise all weights and biases to small values;

while termination not met **do**

```

foreach (x, t) in D do Where x are the inputs and t are the targets
    Apply x to the network and calculate the output of each neurone  $o_u$ ;
    foreach output unit  $k$  in  $n_{out}$  do
        Calculate the error term of the output unit;
         $\delta_k \leftarrow (t_k - o_k) * \frac{d \text{activationfunction}}{d o_k}$ ;
    foreach unit  $r$  not in  $n_{out}$  do
        Calculate the error term of the output unit;
    Update each network weight.

```

When implementing *back-propagation* through the network, one is not guaranteed to find the global minimum of the solution. This highlights the most significant shortcoming of the gradient descent search. Practically, several alterations to the algorithm can improve its performance by avoiding local minima to some extent.

Many algorithms implement a *momentum* factor to the weight updating process. This is done by adding a fraction of the neurone's previous weight update to its next update.

Momentum plays two major roles in finding a minimum. First, it allows the step size to increase when consistently moving towards a minimum. This decreases the number of iterations required for convergence. Secondly, as this momentum term pushes the weight updates in the same direction as the previous iterations', small local minima can often be avoided [17].

Additionally, the algorithm can be modified to update the weights more regularly. This may be done after every training example or after a specified batch size. In the former case, the error term in Equation 21 then becomes:

$$E_d(\mathbf{w}) = \frac{1}{2} \sum_{k \in N} (t_k - o_k)^2 \quad (21)$$

This variation is called *stochastic gradient descent* (SGD), and despite being computationally more expensive, allows for larger step sizes in each iteration of updates. This, together with the fact that each update is now governed by $\nabla E_d(\mathbf{w})$ means that SGD is less prone to converging on local minima. [17].

Previously unmentioned is the stopping criteria for the *back-propagation* algorithm. Intuitively one may expect to terminate the algorithm once $\nabla E(\mathbf{w}) = 0$. However, this condition is rarely met, and performing many iterations of the algorithm causes overfitting of the problem.

Overfitting implies that the trained function has only learned to represent the observed data with no generalisable ability. Practically, an overfitted solution is of little use and therefore the number of iterations must be determined another way. One method of preventing overfitting is to provide the algorithm with a *validation* set in addition to the training set. By evaluating the algorithm on a dataset that it has not been trained on, we can improve generalisation. Importantly then, we can limit the number of training iterations such that the lowest *validation error* is achieved.

2.9 EIT Reconstruction and Computational Intelligence

A wide variety of machine learning algorithms have been applied to the reconstruction problem of EIT. The problem has been modelled as both a classification problem and a regression one using ANNs, support vector machines, genetic algorithms and convolution neural networks. A few relevant works are discussed here.

Adler et al present an early attempt at applying the reconstruction problem using ANNs [18]. Their network uniquely consists of adaptive linear elements (ADALINE) to solve for each element in a FEM (120 elements). Their network is trained using the Windrow Huf algo-

rithm for 1500 iterations, with stopping criteria considering the root-mean-squared value of errors. Several models are trained on simulated data, some of which include different levels of SNR(0 dB, -5 and -10 dB). The authors note that models trained without noise exhibit better spatial resolution than both the back-projected reconstruction and the noisy models, (0.1, 0.25, 0.15 respectively, at half the radial distance to the boundary). The noisy models were more robust to noise and were still able to outperform the back-projected reconstruction algorithm on measured data.

The genetic algorithm has been used in [19] to train a radial basis function (RBF) and directly in [20] to reconstruct an EIT image. Both of these works are restricted to simulated data and lack realistic considerations such as measurement noise.

In previous work on this topic, Crompton used ANNs to determine the location, size and impedance of simulated inhomogeneities as well as to perform the reconstruction algorithm. A reported average location and size error is given as 0.0198, with the reconstruction error for an image from noisy measurements given as $\%|error| > 0.1 = 21.48\%$. An arbitrary noise function is applied to achieve -12 dB SNR in the simulated measured data. The effect of network architecture on the accuracy of reconstructed images was not performed when it is noted that the network designed to detect the location and size of an anomaly outperformed the network designed to reconstruct images. The average absolute errors are 0.0414 and 0.074 respectively [21].

As these networks typically require very long training times, Martin et al propose a novel method of training an ANN using particle swarm optimisation (PSO) [22]. Their PSO trained model converges within 2000 training iterations as compared with +10000 iterations for the SGD model. The models are trained on simulated data with the addition of filtered white Gaussian noise and elliptical models to compensate for electrode placement uncertainty. In simulation the PSO ANN outperforms the one step Gauss-Newton method with a position error of 2.91% compared to 9.37% and a reconstructed resolution difference of 3.16% vs 11.32%. Experimental results from measured data validate their simulated results.

Rymarczyk et all propose another novel approach to improving both ANN training times and performance by using multiple ANNs for the reconstruction problem. In [23] the authors compare elastic nets, LARS and ANNs trained on simulated data against the one step Gauss-Newton reconstruction. They show that after being trained on the same training data, an ANN with fewer output targets has a lower mean-squared-error (MSE) and higher regression (R) than one with many outputs, see Table 1. The networks are trained using the Levenberg-Marquardt algorithm with stopping conditions determined by no changes in MSE of the validation set.

These networks are then applied to measured data and the results show the multiple ANN

Table 1: Comparison of neural networks with 1 and 10 responses. 96-10-1 represents an ANN with 96 input neurones, 10 hidden layer neurones and 1 output neurone. Results taken from [23].

Quality Indicator	96-10-1	96-20-10	96-10-10
MSE	0.0069	0.0086	0.0087
\bar{R}	0.7548	0.6897	0.6994

structure is significantly better than all other tested reconstruction methods for any configuration of electrodes and number of inhomogeneities. The ANN reconstructed images are visually more accurate but exhibit spikes of noise.

The performance metrics used were the MSE, relative image error (RIE) and image correlation coefficient. The displayed superiority of the ANN network is questionable as the ANN networks were trained on larger training sets with more elaborately simulated data than the other networks. In the 16 electrode experiment with two objects in the test tank, the ANN has a MSE of 0.0074 as compared to the next lowest MSE of 0.0111 by the elastic net.

3 SYSTEM DESIGN

This project necessitates the design of an EIT system to produce measurement data, as well as a machine learning (ML) algorithm to perform the reconstruction process. This Section begins by motivating the need for such a system and outlines the specifications for this system. The design choices for the hardware system and the ML algorithm are also discussed. An investigation into the design of an EIT hardware system was performed in prior work. The design was not completed to the point where an image could be reconstructed. This project builds on the work done previously.

3.1 Needs and Motivation

This project aims to show that the EIT inverse problem can be performed by an ML algorithm on measured data but trained on simulated data. No such hardware system was readily available, therefore necessitating the design and implementation of a simple time-division multiplexed (TDM) EIT system. As the simplest EIT configuration, a TDM system is ideal for the allocated time-period and project budget.

The reconstruction problem is non-linear, computationally expensive and requires *a priori* information to solve. It is therefore desirable to implement an ML algorithm capable of

solving the inverse problem with no required assumptions. This necessitates the design and implementation of a suitable ML algorithm.

3.2 *Specifications*

Medical EIT systems have many technical requirements, namely pertaining to image frame rate, maximum rated current injections and safety mechanisms. However, this simple construct aims to serve as a proof of concept and will not be tested on humans. This widens the design space. Practical application will serve as a guideline to the system specification. The specifications of the system are divided into functional and non-functional categories.

3.2.1 *Functional Specifications*

The device's functional specifications are defined as:

- FS0:** The applied current must equal 1 mA, with a precision of $\pm 5\%$ over the expected load impedance range¹.
- FS1:** The system must apply a single excitation frequency, f_s in the range $[0.3; 10] \text{ kHz}$.
- FS2:** The measurement system detection range must be within $\pm 5 \text{ V}$.
- FS3:** Image reconstruction (which includes measurement process) must take less than 10 s to perform.
- FS4:** An image reconstructed from measured data must faithfully depict the physical system.
- FS5:** The system must use 16 electrodes for current stimulation.

3.2.2 *Non-functional Specifications*

The cost of implementation should be minimised. This should be achieved through conservative use of components and efficient design. This is especially true if the final system is intended to be portable and lightweight and accessible.

¹The tank is filled with a saline solution [$\approx 55 \text{ S/m}$] [24], therefore the output load is expected to be within $[1; 10] \text{ k}\Omega$.

3.3 Hardware Concepts

Many of the components required for this system are readily available, due to previous work in the field by Tšoeu et al [25] [26]. For this reason, these components have been preferred in the design process. This section will discuss two potential designs for a simple EIT TDM system.

3.3.1 Single-Source System

The main design process for the single-source system is described in Appendix ???. The initial design utilises an Arduino as the control unit. This introduces several issues, namely the Arduino's insufficient sampling speed, the unipolar restriction of the Arduino's internal ADC and the Arduino's 10-bit ADC resolution. This only allows for a $40/2^{10} = 3.9\%$ boundary voltage detection sensitivity and a maximum excitation frequency of ≈ 300 Hz.

This design addresses the ineffectual control unit by replacing the Arduino with a USB30D μ DAQ data acquisition card produced by *Eagle Electronics*. The μ DAQ has 32 multiplexed, bipolar analogue input channels with a maximum 1 MHz sample rate. In a 16 electrode system, this gives an effective system-wide sample rate of 62.5 kHz.

The μ DAQ accepts analogue input signals of ± 5 V, for this reason, the variable gain instrumentation amplifiers are important for appropriate scaling of the differential signals. Unfortunately, the μ DAQ only has 3 DIO ports, which are necessary for coordination of the multiplexers. The design implements four 8:1 (ADG508F) multiplexers to distribute the dual-ended current supply to the 16 electrodes. Each multiplexer has three select lines $S_{0:2}$, and one enable line En . The design is configured to reduce the number of redundant control lines. Five control bits are required, and therefore an Arduino is used in the final design, seen in Figure 13.

The design is summarised as follows:

- **Oscillator:** The voltage signal used to drive the VCCS comes from an external signal generator (Keysight EDUX1002G digital oscilloscope).
- **Current source:** An enhanced mirrored Howland current source (EHMCS) has been implemented using high impedance JFET operational amplifiers (LF531) and $\pm 1\%$ tolerance resistors.
- **Multiplexers:** Two 8:1 ADG508F multiplexers are connected to form a single 16:1 unit. Both 16:1 units are used to source/sink current to/from the EMHCS.
- **Phantom:** A circular Plexiglass tank holds 32 copper electrodes arranged around a circular tank in a single plane. The tank has a height of 5 cm and a diameter

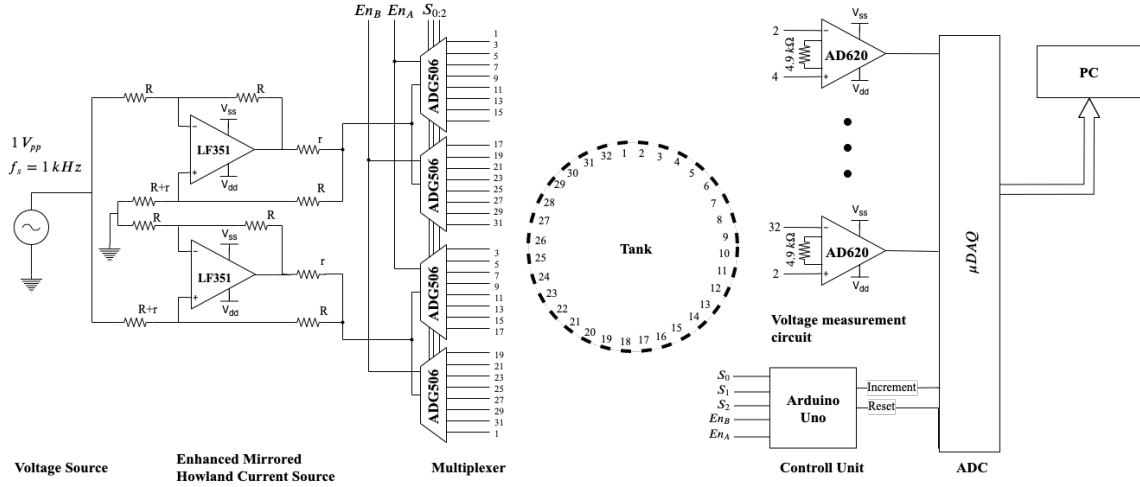


Figure 13: Single-source EIT hardware system design.

of 22 cm. Current sources are connected to every other electrode (16 electrodes) and voltage measurements are made on all non-current conducting electrodes (16 electrodes).

- **Voltage measurement:** 16 AD620 instrumentation amplifiers are connected to each adjacent pair of electrodes (differential configuration), each with a gain of 2. This gives 16 measurements for each stimulation.
- **Arduino Uno:** Used to coordinate the multiplexers. Increments the control signal with each pulse from μ DAQ or resets to channel 0.
- **ADC:** The μ DAQ USB30D is connected to the outputs of each instrumentation amplifier and transmits the measured results serially.

This tank configuration is not standard as the electrodes are uni-functional. Odd electrodes are solely used for current injection and even electrodes are solely used for measurements. This interleaved configuration has three advantages. Namely, differential voltage measurements can be obtained across the active pair where the current density and therefore sensitivity is highest (1), a full measurement set (256 measurements) is obtained, thereby increasing the number of independent measurements (2), and no additional circuitry is required to isolate the current source and measurement circuits (3).

3.3.2 Multiple-Source System

The non-ideal nature of multiplexers has the potential to negatively impact system performance through non-idealities. This design approach minimises the number of required multiplexers. Conversely, this design requires 16 mirrored current sources, drastically

increasing the build complexity of this design. Furthermore, this design must take into account output impedance matching between current sources to ensure isotropic stimulations. This design also preconditions the measured signal by filtering out high-frequency noise.

The design is based on the single-source system. The changes are summarised as follows:

- **Current source:** 16 enhanced mirrored Howland current source (EHMCS) implemented using high impedance JFET operational amplifiers (LF351) and $\pm 1\%$ tolerance resistors.
- **Multiplexers:** Two 8:1 ADG508F multiplexers are connected to form a single 16:1 unit. The voltage signal is multiplexed to each of the current sources.
- **Signal Conditioning:** A fourth-order active low-pass filter, preconditions each differential voltage signal. The filter cut-off frequency is placed at $f_c = 2f_s$.

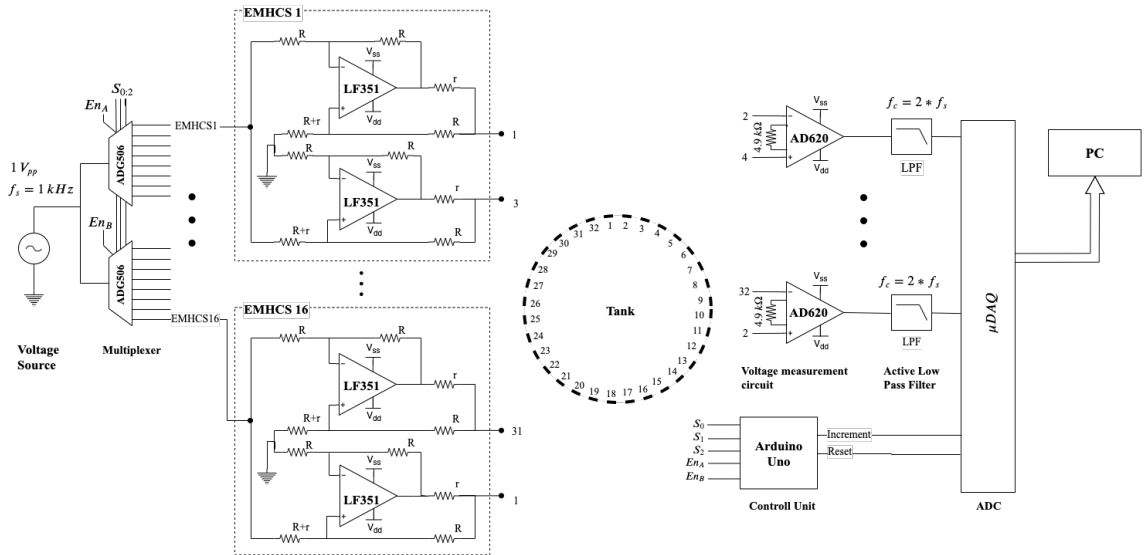


Figure 14: Multiple-source EIT hardware design.

Based on the build complexity, component requirements and time limitations, this design is not be realised.

3.4 EIDORS Models

The EIDORS model represents the physical system in simulation. An accurate representation of the system is imperative for the simulated results to converge with the experimental results.

To illustrate the importance of this similarity we may consider how an EIT image is reconstructed. First EIDORS estimates a conductivity distribution, then iteratively calculates the forward problem, comparing the resulting boundary voltages with the measured voltages and then adjusts the conductivity set. If the forward model does not sufficiently represent the physical system, the correct conductivity distribution cannot be estimated and the resulting image is an unfaithful depiction. This section first describes the data structures used by EIDORS before defining two model representations of the system.

3.4.1 EIDORS Structures

The EIDORS software package is written in *Matlab* and includes a number of inbuilt functions and data structures used to reconstruct EIT images. The authors have employed a somewhat object orientated approach to define four main objects (stored as structures in *Matlab*): `fwd_model`, `inv_model`, `data` and `image`. The relation of these objects can be seen in Figure 15 [27].

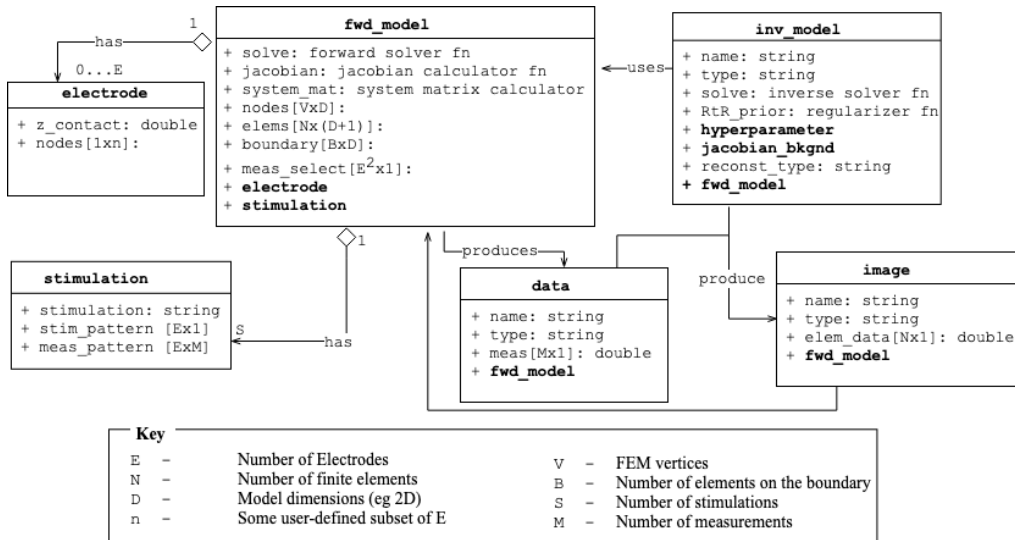


Figure 15: Entity relation diagram of the structures used by EIDORS. Some irrelevant structure members have been excluded. E

The `fwd_model` is the most complex object and is used to produce the boundary voltages. The `fwd_model` uses a number of `stimulation` structures to specify exactly how the boundary voltages are produced and measured. This allows us to specify the applied current amplitude levels, driving pairs (`stim_meas`) and measurement pairs (`meas_pattern`) for each stimulation in `S`. To account for non-ideal electrodes in a system, EIDORS permits the user to define complex impedances for an individual electrode, as defined in the `electrode` array.

Once defined, the `fwd_model` is used to calculate a frame of data. The resulting measurements are stored in a `data`-type object. A frame of data consists of all the measurements made in each stimulation, arranged sequentially.

To reconstruct an image we define the `inv_model` and specify either static or difference reconstruction (`recon_type`), the reconstruction algorithm to use (`solve`), the regularisation function (`RtR_prior`) and the associated hyperparameters (`hyperparameters`). Reconstructing a difference image from two `data` objects (homogeneous and inhomogeneous) and the `inv_model` produces an `image` object.

The `image` object is the simplest structure and holds the conductivity values for each element in the FEM.

3.4.2 16-Electrode Model (E16)

In this configuration, the simulated model represents a system with 16 electrodes. To match the physical 256 measurements, differential voltage measurements are made on all electrodes (including current-carrying electrodes). The stimulation and measurement pattern is shown in Figure 16

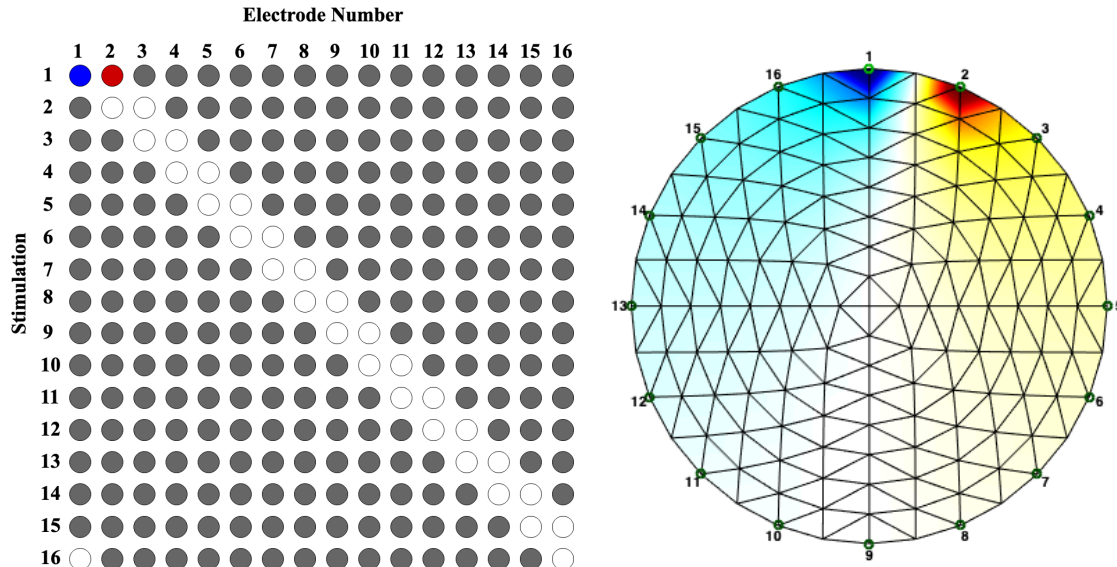
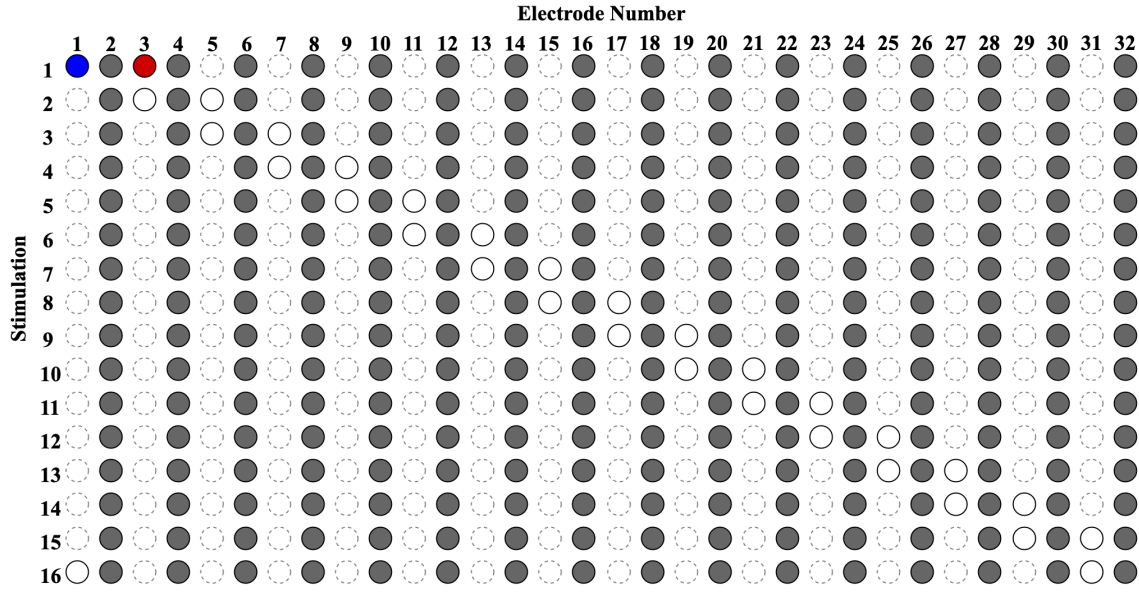


Figure 16: Stimulation-measurement pattern for the 16 electrode model.

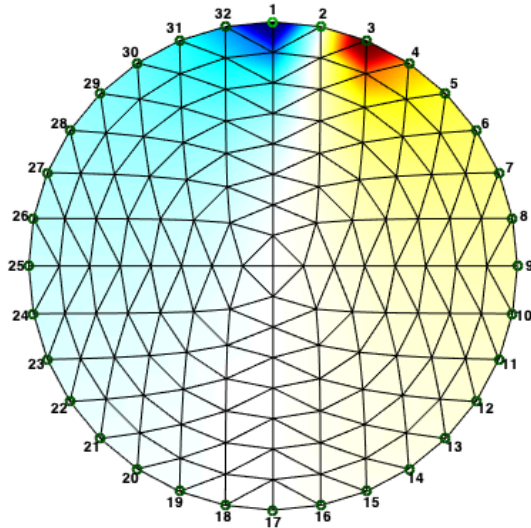
The drive current amplitude is set at 1 mA and the background conductivity is arbitrarily set to 1Ω .

3.4.3 32-Electrode Model (E32)

The physical phantom has 32 electrodes, which are configured as 16 current injecting electrodes interleaved with 16 voltage measuring electrodes. The stimulation and measurement pattern still results in 256 measurements but here the voltage measurements are not performed on current carrying-electrodes. Figure 17 depicts the proposed stimulation-measurement pattern.



(a) White circles indicate current injecting electrodes and faded circles are unused electrodes. Grey circles represent measurement electrodes, made on all adjacent evenly numbered electrodes. Each row represents a stimulation.



(b) EIDORS FEM of the first stimulation.

Figure 17: Stimulation-measurement pattern for the 32 electrode model.

The current amplitude is set to 1 mA and the background conductivity is arbitrarily set to 1Ω .

3.5 Machine Learning Algorithm

The process of implementing an effective machine learning algorithm begins with a well-defined problem.

Task: Perform the EIT inverse problem to determine the internal conductivity distribution from a set of 256 simulated boundary voltages. This involves mapping the L_{sm} boundary voltages (a function of the stimulation/measurement pattern) to N conductivity values of a FEM.

Input Data: L_{sm} boundary voltages. These are continuous voltage variables.

Network Output: A set of estimated conductivities $\{\sigma_{net}\}$ represented in an $N \times 1$ array.

Target Output: The set of simulated conductivities $\{\sigma_{sim}\}$ used to generate the measurement data, in an $N \times 1$ array.

Performance Metric: A network's performance will be measured by the mean-squared-error (MSE) of the learned function's output and the target output.

Let us define a sparse FEM with only 256 elements to limit the size of the hypothesis space H . The conductivities are continuous variables, so a regression type algorithm is used. The problem is summarised in Figure 18.

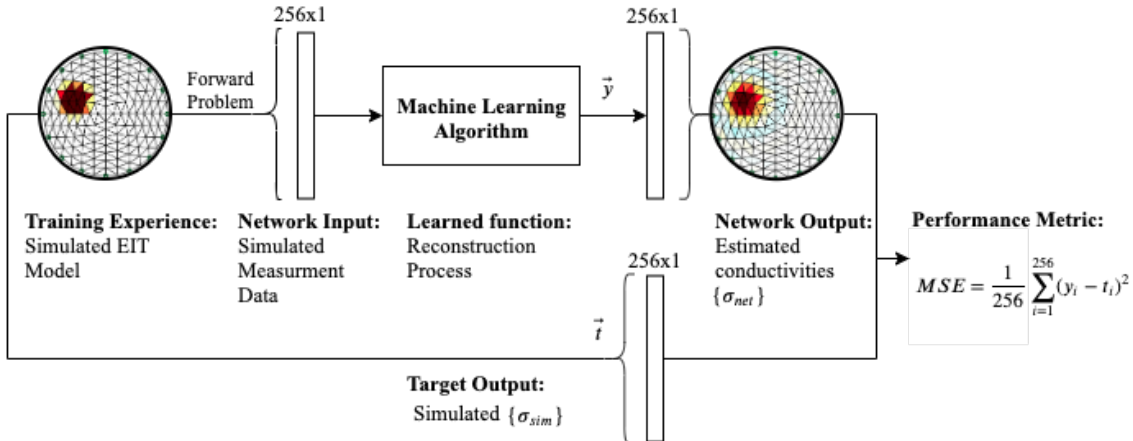


Figure 18: The proposed machine learning problem.

The format of the task presented dictates a non-linear mapping of real-valued boundary voltages to real-valued conductivities. This necessitates a regression-type algorithm. This problem is therefore ideally suited to an ANN. For these reasons, and based on the promising results of [23] [21], an ANN architecture is chosen for the task.

ANNs are expected to provide rapid interpretations of the applied inputs once the task has been learned, but are not the fastest algorithms [23]. Even so, this project focuses on the

reconstruction quality and is less concerned with the attainable frame rate.

Extensive training times due to the large H space are a significant disadvantage of ANNs. To limit the training time, a shallow ANN with a minimum number of hidden layer neurones will be chosen. This is motivated by the fact that a single hidden layer with a sufficient number of hidden layer nodes has enough embedded complexity to represent any non-linear function [17].

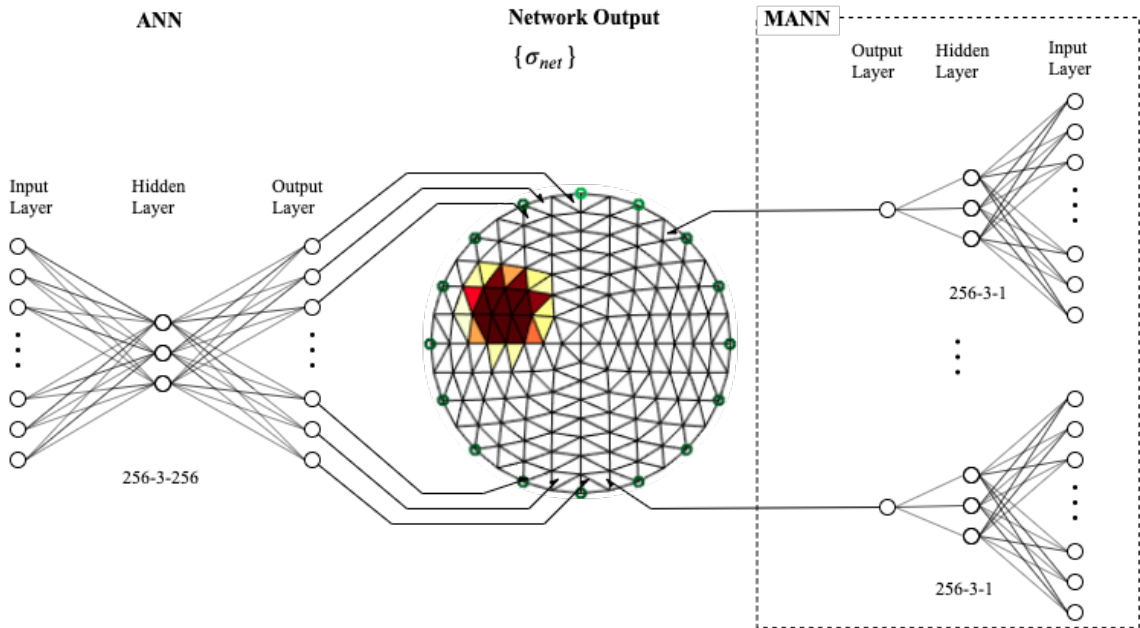


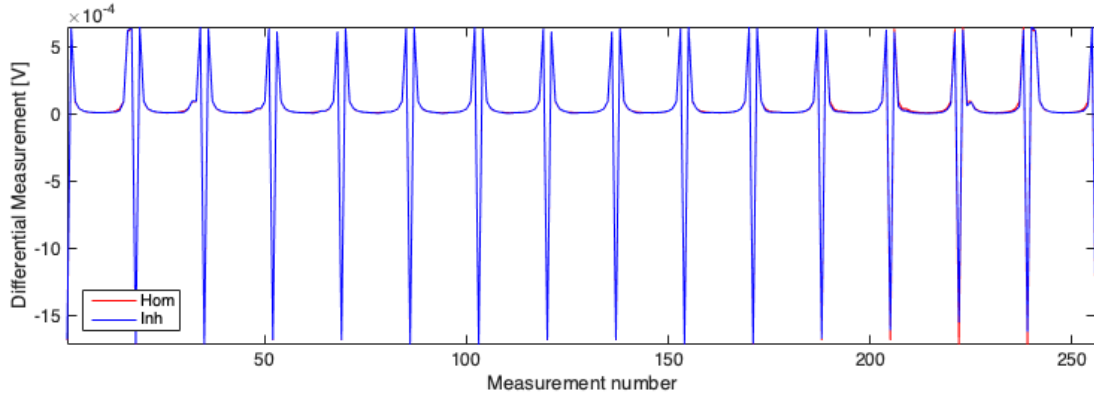
Figure 19: Classic ANN architecture as compared with the multiple ANN architecture proposed to solve the EIT reconstruction problem.

An extension of the classic ANN architecture will also be implemented. This architecture decomposes a $256 \times X_{ANN} \times 256$ ANN into N individual ANNs of the form $256(256 \times X_{MANN} - 1)$ and is inspired by [18] and [23]. Each ANN is then responsible for a single conductivity in the $\{\sigma_{net}\}$, which reduces the number of hyperparameters in each network and consequently reduces training time. Additionally, as the entire measurement set is used to deduce a single value, the problem becomes well defined.

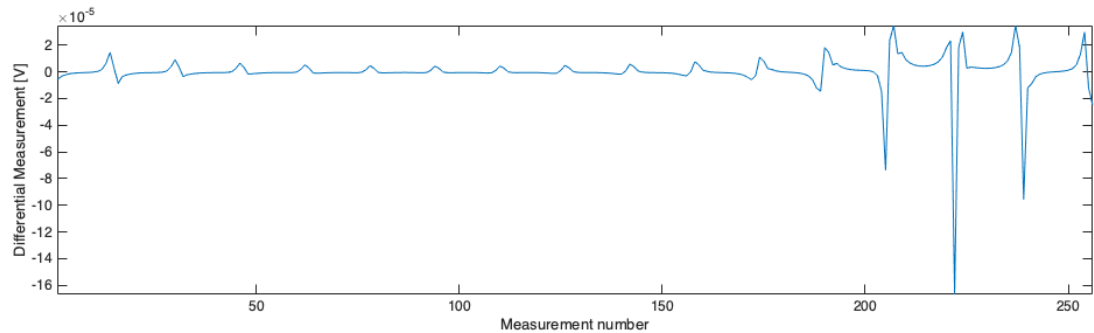
The ANNs will be trained on a variety of learning algorithms, which include *Adam*, *Levenberg-Marquardt* (LM) and classic *Stochastic Gradient Descent* (SGD).

3.5.1 Input Data

To understand the format of the input data, let us consider the resulting boundary voltages for the 16 electrode model² in the homogeneous and inhomogeneous cases. To do this, we create the E16 model, calculate the forward problem to obtain the *homogeneous* boundary measurements, simulate an inhomogeneity in the tank, and then perform the forward problem again to obtain the *inhomogeneous* measurements.



(a) Homogeneous and inhomogeneous boundary measurements obtained from the E16 EIDORS model.



(b) Difference between the homogeneous and inhomogeneous boundary measurements.

Figure 20: ML algorithm input data profile for the E16 model.

Figure 20a illustrates the so-called *U-curve* plots for both measurement sets. To appreciate the inhomogeneity's effect on the boundary voltages we plot the difference between the sets, as in Figure 20b.

The greatest difference at the boundary voltage occurs nearest to the object, and the subsequent change is dependant on the conductivity of the object. Therefore, the difference

²A similar analysis of the 32 electrode model (E32) can be found in Appendix B

signal effectively conveys the size, position and conductivity of the inhomogeneity. Furthermore, the range of the difference signal is far smaller than the inhomogeneous measurement range. For these reasons, the difference signal is chosen as the network input.

The input signal is normalised before entering the network. This ensures a uniform input signal range for the network and may contribute to a decreased training time [28].

3.5.2 Output Data

The output data format can be analysed similarly. By solving the inverse problem for the E16 model we obtain the conductivity distribution for each of the elements in the defined mesh, $\{\sigma_{inv}\}$. The estimated $\{\sigma_{inv}\}$ is, of course, dependent on the choice of inverse solver. We will consider the *Gauss-Newton one step* iterative numerical method with a *Tikhonov* image prior as it only requires a single iteration and produces a clear reconstruction.

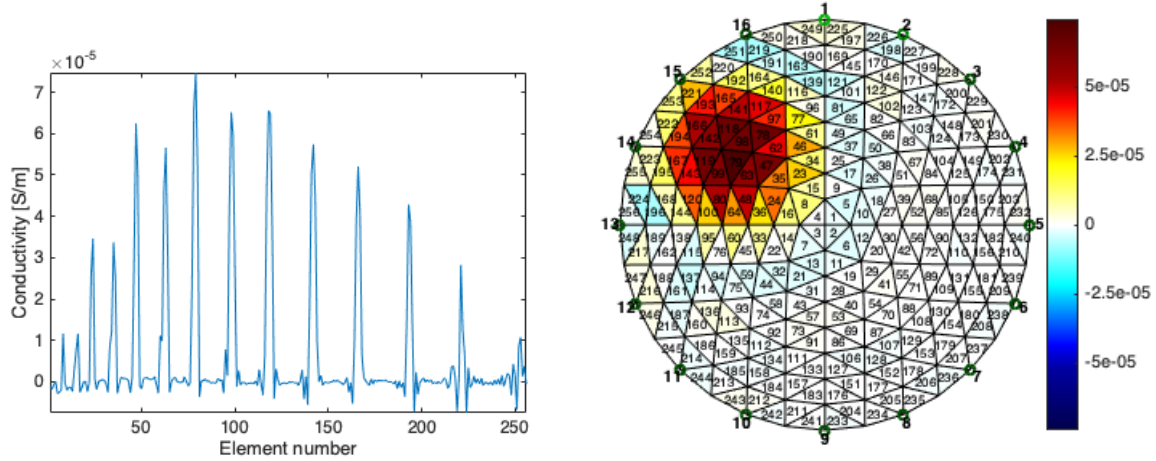


Figure 21: ML algorithm output data profile.

3.5.3 Training Data

Machine learning (ML) algorithms learn from experience, in the form of training data. The training data provides a porthole through which the algorithm may view the task. The quality and size of the training data, analogously represent the clarity and size of the porthole.

There is no strict rule that dictates the required amount of data for any specific ML algorithm. As the complexity of a model grows, so too does the number of model parameters and consequently, the amount of training data required. This is commonly known as *the curse of dimensionality*.

The number of hyperparameters in the model, therefore, provides a good indication of the training data size. A shallow fully connected 256-10-256 ANN has 71 178 tuneable hyperparameters. Therefore, the training data should contain a comparable number of training examples.

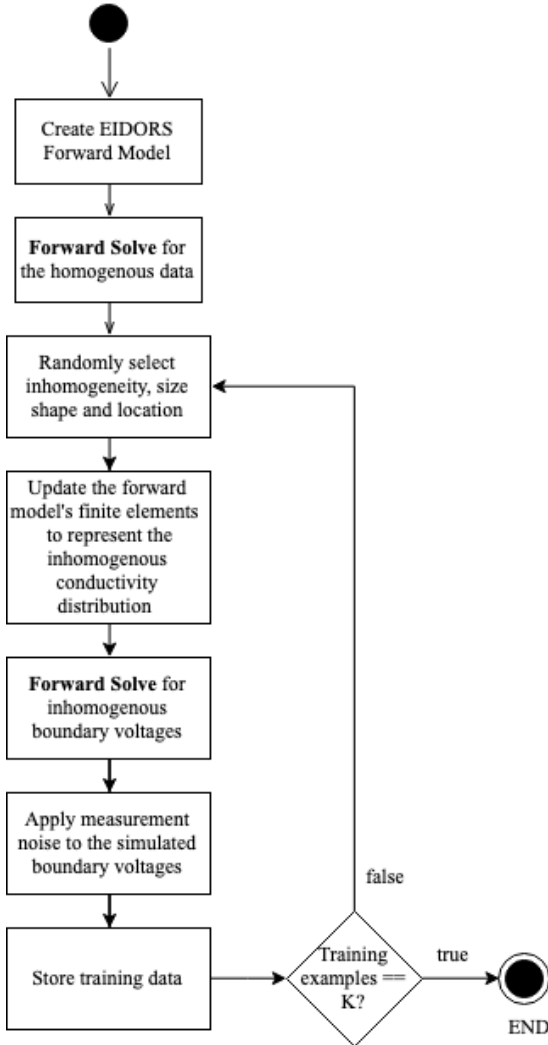


Figure 22: Flow diagram showing the generation of K simulated training examples for a ML algorithm. K is set to 50 000.

Figure 22 shows the flow of the simulated training data generation program. A training set

is produced for both the E16 and E32 models and features a single circular inhomogeneity that is randomly sized and randomly placed within the simulated tank.

Each training example is a pair of input/output data structures. The *input* data is the difference signal (*homogenous measurements - inhomogeneous measurements*) and the *output* data is the actual $\{\sigma_{sim}\}$ describing the inhomogeneity. The reconstructed set $\{\sigma_{inv}\}$, is not used for training as this would limit the performance of the algorithm to the best estimate of the classical reconstruction.

3.6 ANN Parameters

The proposed ANN is restricted to a shallow network structure in the form 256-X_{ANN}-256. The design parameters under consideration include:

Hidden Layer Activation Function: [*tanh*, *sigmoid*, *relu*]

Hidden Layer Neurones X_{ANN}: [5, 10, 15, 20]

Output Layer Activation Function: [*purelin*, *relu*]

Training Algorithm: [*LM*, Adam, SGD]

The *optimal network parameter configuration* is obtained heuristically through an iterative process. A Python script using the *TensorFlow* and *Talos* libraries is used to automate the process of training and evaluating each permutation. Due to the considerable amount of training involved in the experiment, a subset of the training data is used (10 000 examples). The networks are compared based on their validation loss. The optimal parameters are then used to train the networks on the full data set, including early stopping parameters which monitors the change in validation loss. A 15% split of the input data is used as the validation set to reduce the chance of overfitting.

As the *LM* training algorithm is not supported on *Keras* models, it is tested using the *Matlab* neural network toolbox.

3.7 MANN Parameters

The multiplicity of this architecture makes a direct evaluation of the network impractical. More importantly, since the MANN is an extension of the ANN, the optimal design parameters are expected to carry over, excluding X_{MANN}.

The optimal X_{MANN} is found by applying the ANN optimal parameters to three permutations of X_{MANN}, [5, 10, 20]. Testing reveals optimal results with X_{MANN} = 10.

4 SYSTEM TESTING

This Section demonstrates the testing used to ensure that each of the subsections is functional or where the system is deficient. In each case, the methodology is described. The tests are conducted in a modular fashion to ensure that each subsystem functions as expected.

4.1 Hardware performance

The hardware system testing is broken down into each of the hardware components which are tested individually to ensure their functionality.

4.1.1 Current Source Stability

This test examines the output characteristics of the EMHCS under different load resistances and for different frequency ranges. In TDM the current source frequency is constant but the load impedance is variable. As such this experiment only investigates the source stability with changes in the load. The experiment is first simulated to verify the design (Figure 23b), and then tested experimentally.

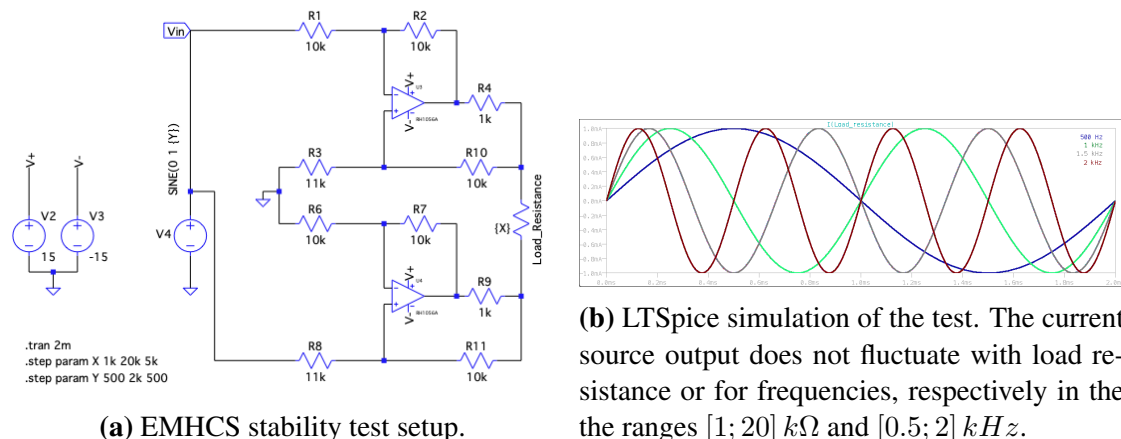


Figure 23: EMHCS simulation.

The EMHCS is configured as in Figure 23a using two J-FET LF351N amplifiers and $\pm 1\%$ resistors to produce 1 mA across the load.

Table 2: Current source stability with variations in load at set frequency.

	300 Hz	600 Hz	1 kHz	2 kHz
SD	0.0339	0.0404	0.0390	0.0424
MEAN	1.0088	1.0008	1.0051	1.0071
MSE	0.0011	0.0015	0.0014	0.0017

The current source is excited by a $1V_{pp}$ sinusoidal voltage generated externally. The load current is measured between the current source and the load resistance for a range of load resistances ($\pm 5\%$ tolerances) and excitation frequencies. The resulting sinusoidal current amplitudes are shown in Figure 24.

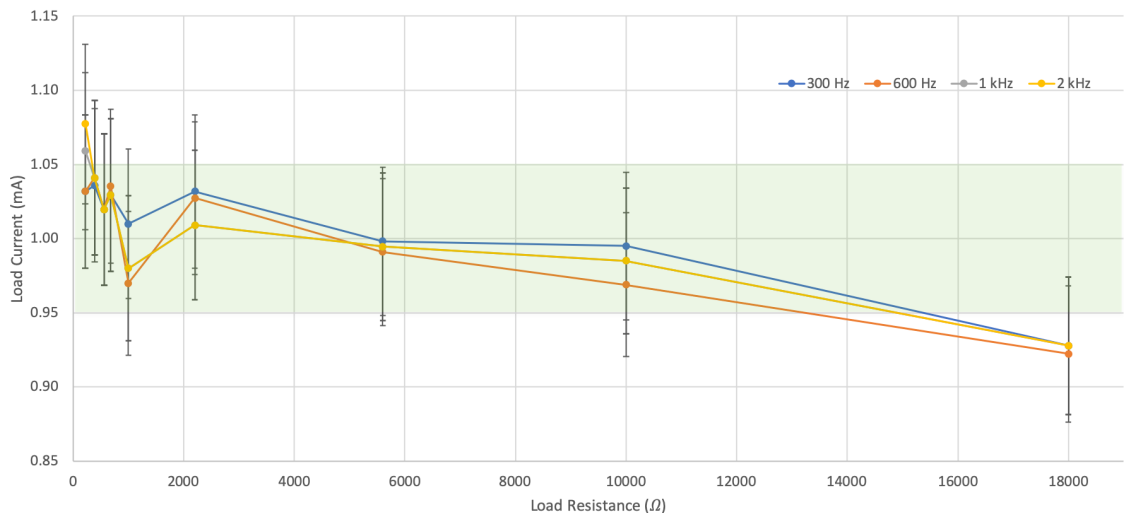


Figure 24: Measured sinusoidal current amplitude through a range of load resistances driven by a 1mA EMHCS. The green band represents a precision of 5%, and 5% error bars are applied to the data points.

Table 2 shows the current source stability over a range of loads at each frequency. A current source is precise if the standard deviation (SD) and mean-squared error (MSE) are low, but a mean current draw closest to 1 mA is evidence of an accurate source. The experiment reveals that the current source is most precise at 300 Hz, but most accurate at 1 kHz.

If we consider the MSE as a measure of precision³, then all frequencies meet the requirement **FS0**. However, the system only meets the required accuracy at 600 Hz and 1 kHz.

³A MSE of 0.0011 implies that the current lies on average, within $\pm 0.11\%$ of the desired current.

Table 3: Truth Table for the control unit outputs. E_{i-j} represents the electrodes i and j connected to the current source through the multiplexing circuit.

	S_2	S_1	S_0	En_A	En_B
E_{1-3}	0	0	0	1	0
E_{3-5}	0	0	1	1	0
E_{5-7}	0	1	0	1	0
E_{7-9}	0	1	1	1	0
E_{9-11}	1	0	0	1	0
E_{11-13}	1	0	1	1	0
E_{13-15}	1	1	0	1	0
E_{15-17}	1	1	1	1	0
E_{17-19}	0	0	0	0	1
E_{19-21}	0	0	1	0	1
E_{21-23}	0	1	0	0	1
E_{23-25}	0	1	1	0	1
E_{25-27}	1	0	0	0	1
E_{27-29}	1	0	1	0	1
E_{29-31}	1	1	0	0	1
E_{31-1}	1	1	1	0	1

4.1.2 Control Unit

In this design, the control unit coordinates the multiplexer switching to connect the current source to a pair of electrodes. The Arduino fulfils this role and serves as an extension of the μ DAQ’s digital output pins. The *active* pair of electrodes is related to the control signal according to Table 3.

This subsystem is a simple binary up-counter that increments or resets in response to an appropriate interrupt. The program operation is shown in the Figure 25.

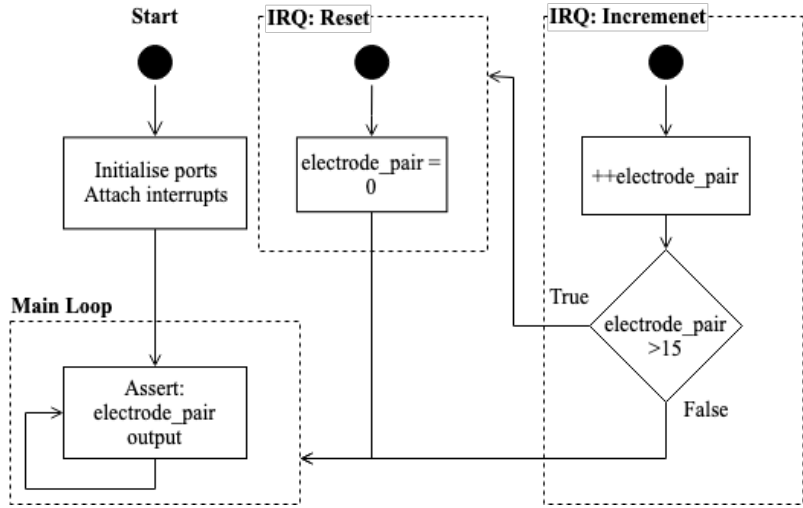


Figure 25: UML activity diagram of the control unit program running on the Arduino.

To test the control unit, a set of five LEDs are connected to the digital outputs. A low-frequency pulse wave services the *increment* interrupt pin and a push-button is attached to the *reset* interrupt pin. The LED configuration is seen to match the truth table with each increment and resets to zero when the push-button is used.

4.1.3 Multiplexed outputs

As the signal gate, we expect the multiplexer to behave as an open circuit between the input and output ports that are not selected. This means that for a selected electrode pair E_{i-j} , the multiplexer input signal must ideally be confined to these two electrodes.

To test the multiplexer's off-channel signal rejection, the current source is connected to the multiplexer as in Figure 13. The current source is excited with a $1V_{pp}$ sinusoid at $f_s = 1\text{ kHz}$, and the control unit is used to toggle through each of the active electrode pairs.

The voltage profile across the multiplexer for each of the 16 stimulation patterns is recorded with the μ DAQ. The voltage profile of four stimulation patters is shown in Figure 26.

The experiment indicates that the multiplexer lines are not completely isolated. The unexpected presence of voltage on neighbouring electrodes implies an accompanying current flow. The system's failure to restrict current to the active electrode pair is expected to impact on the quality of the measurement data.

This may be attributable to the unpredictable current flow as additional electrodes be-

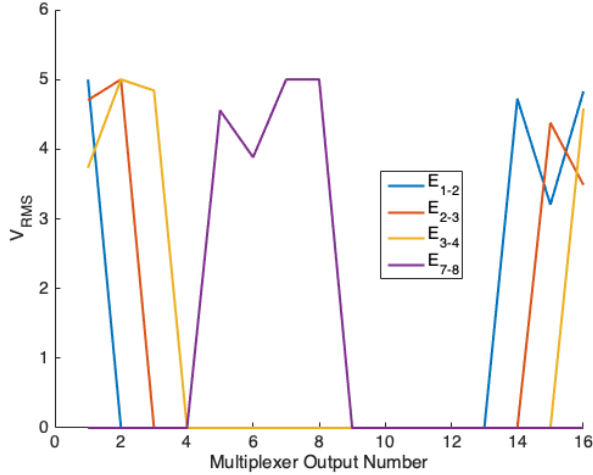


Figure 26: RMS voltage profile across each of the multiplexer outputs, shown for four active pairs, E_{1-2} , E_{2-3} , E_{3-4} and E_{7-8} .

come *active* (in addition to E_{i-j}). Additionally, this means that the Neumann boundary condition no longer holds true, and the forward problem's solution becomes arbitrary.

4.2 Measured data

The data measurement process is facilitated by a *C++* program written in *Visual Studios Code*. The μ DAQ's ADC records voltage measurements and transmits the results serially to a PC. The sampling frequency, sampled channels and number of samples can be set programmatically or using the GUI generated in *Visual Studios Code*. The program also facilitates data logging for each of the 16 channels, which are stored in text files and processed in *Matlab*.

For these experiments the ADC sample frequency, f_{DAQ} , is set at 10 kHz and 200 samples are collected on each channel unless stated otherwise. The measurement process takes roughly $3200/10000 * 16 = 5.12$ s to complete.

Figure 27 shows how the measured data is formatted into a set. Each frame represents the differential measurements taken during an applied stimulation pattern. Since the raw data at the output is time-varying, the root-mean-squared (RMS) value is used.

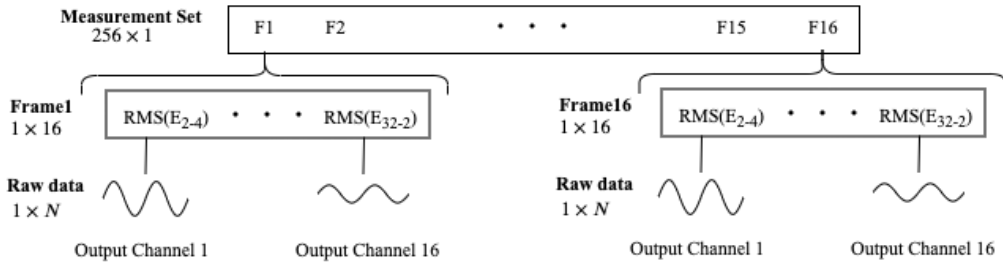


Figure 27: A full measurement set for the EIT hardware system.

4.2.1 Measurement Noise

The system has many IC components, each of which introduce noise to the measurement process. This experiment quantifies the system noise by measuring the outputs of the voltage measurement circuit⁴, in response to a zeroed input signal.

The system is setup as in Figure 13 with $V_s = 0 V$ and a full measurement set is recorded.

Figure 28a shows the noise characteristics of each channel in the first frame. A set of scaled normal distributions illustrate the different offsets and the relative variances of each channel's noise. Analysis of subsequent frames reveal the same trends, implying consistent noise profiles on each channel.

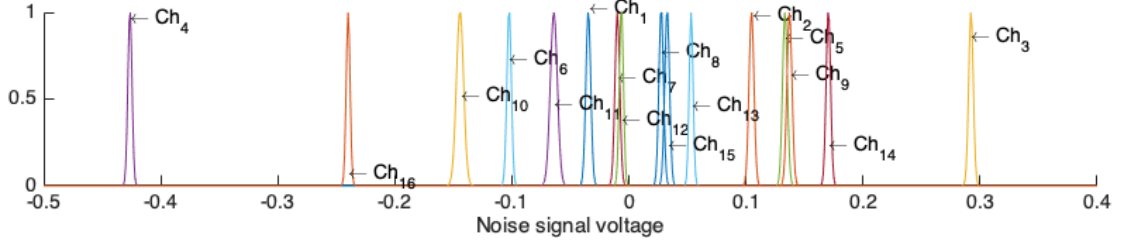
Figures 28b and 28c characterise the noise system-wide. This entails averaging the noise seen on each channel and then averaging throughout each frame. These averages are then fit to a normal distribution. The same procedure is applied to characterise the channel variance.

On average, the channels have a slight negative offset and there is a relatively large spread in the offset across the channels. This is illustrated by Figure 29 which shows the averaged offsets on each channel across the measurement set. These offsets are relatively benign and can be compensated for in software.

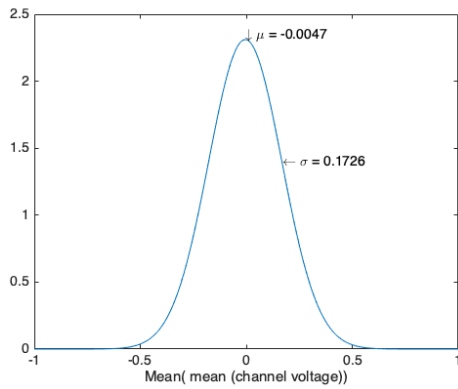
The bandwidth of the measured noise is limited by f_{DAQ} . A frequency analysis of the signal (Figure 30) shows that the noise has the highest power at DC with no considerable contribution from any other singular frequency. Therefore, the system noise can roughly be described as non-zero mean band-limited Gaussian white noise.

A comparison of the signal relative to noise power is measured using the signal to noise ratio (SNR). The SNR is computed using the average signal power on each channel, where

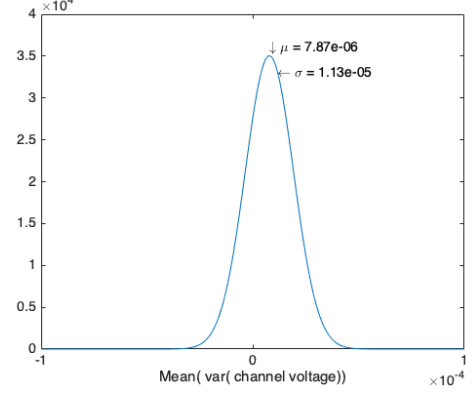
⁴These are the 16 differential voltages made on adjacent even electrodes. Hereon referred to as output channels 1:16



(a) Scaled normal distribution of the noise signal on each output channel of the EIT system, ($S_{0:2} = 000$).



(b) Normal Distribution of the average noise level on each channel.



(c) Normal distribution of the average variance of noise signals on each frame.

Figure 28: Statistical analysis of the measured EIT hardware noise.

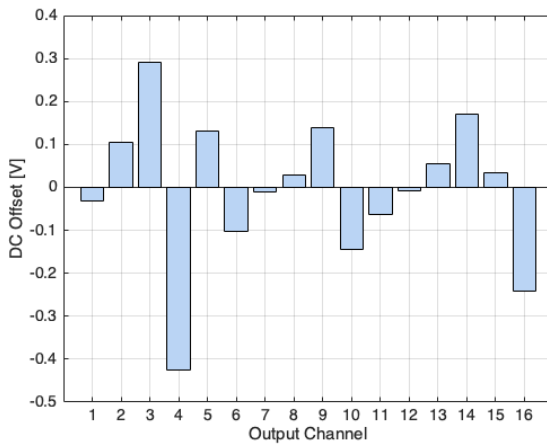


Figure 29: EIT system DC offsets.

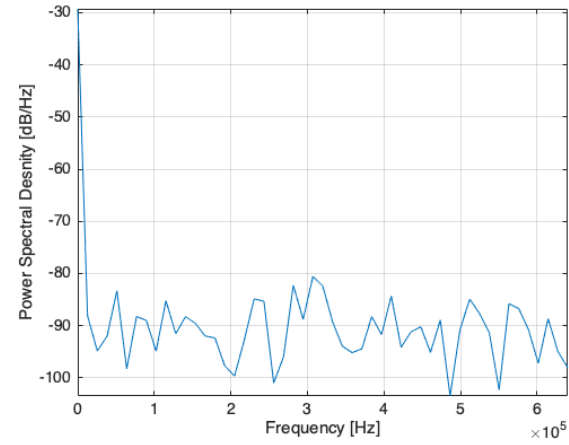


Figure 30: Power Spectral Density of the signal noise.

$SNR = 10\log_{10} \left[\frac{P_{sig}}{P_{noise}} \right]$. Since the signal source is sinusoidal, $y = a\cos(2\pi ft) + c$, the average signal range estimates the amplitude. The signal power is calculated as $P_{sig} = a^2/2$. The SNR is calculated using a homogeneous measurement set⁵ three separate sets of noise measurements. The results are averaged together and shown in Figure 31.

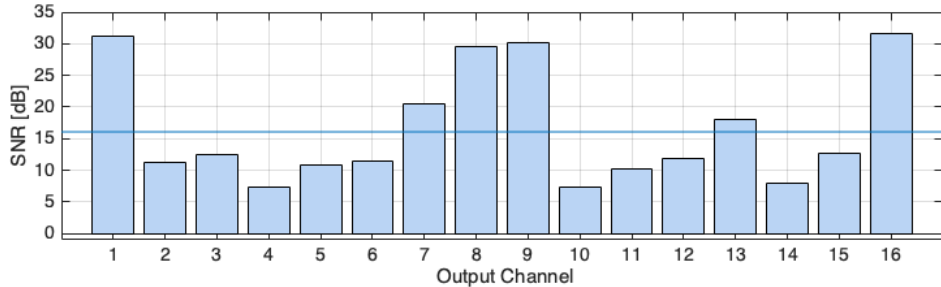


Figure 31: Signal to noise ratio (SNR) for each channel in the EIT system. The blue line indicates the average $SNR = 16.08$ dB.

The system SNR (an average of each channel) is approximately 16 dB with the worst SNR of 4.2 dB on channel 10 and the best SNR of 31 dB on channel 16. The system's non-uniform SNR profile means that the system's sensitivity is also non-uniform. From these results, it would appear that the system is most sensitive to changes near electrodes $E_{15:2}$ and $E_{7:11}$.

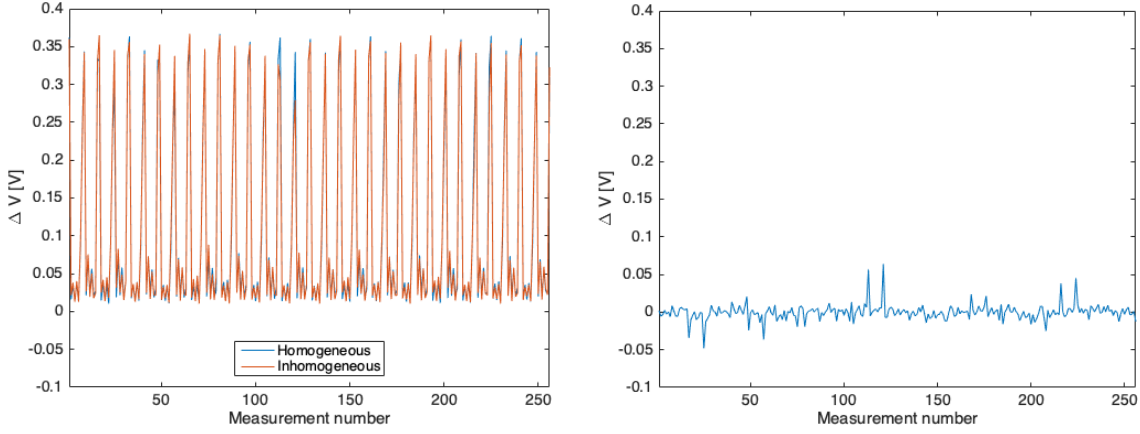
4.2.2 EIDORS Reconstruction

This final hardware test evaluates the system's ability to detect changes in the boundary voltage with some change in the internal conductivity. Indirectly, this proves whether the system is capable of producing measurements that lead to intelligible reconstructions.

The integrated system is connected as in Figure 13 with a $1V_{pp}$ 1 kHz sinusoidal excitation signal applied. The tank is filled with a saline solution and the output channels are sampled at 10 kHz with 200 samples taken on each channel.

A homogeneous measurement is conducted three times to obtain an averaged homogeneous measurement set, effectively reducing the impact of noise in the system. The RMS value of the measurements on each channel are obtained and arranged sequentially to form the *U-curves* seen in Figure 32.

⁵ Obtained using an $1V_{pp}$ sinusoidal input signal at $f_s = 1$ kHz.

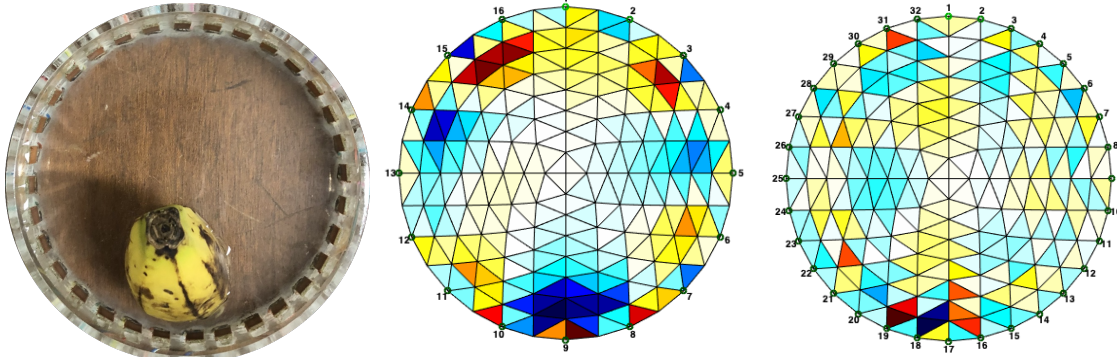


(a) Homogeneous and inhomogeneous measurement data obtained from the EIT hardware setup. **(b)** Signal difference plot showing discrepancies almost midway in the measurement set.

Figure 32: EIT experimental measurement data

The measured *U-curves* do not match the E16 simulated *U-curves* as there are 32 distinct *U*'s and the measurements between the peaks are much lower than in simulation. The measured voltages are also three orders of magnitude larger than in simulation. This likely due to voltage measurement circuit's gain factor and the higher load resistance of the tank solution.

However, the difference plot indicates that the system has detected an anomaly of some shape or form. The E16 and E32 models are both generated and used to solve the inverse problem on the measured data. The resulting images are shown in Figure 33.



(a) Banana placed at 12 o'clock, near electrode E_1 .
(b) E16 model reconstruction.
(c) E32 model reconstruction.

Figure 33: EIT reconstruction from measured data.

The reconstruction quality is poor and neither models produce a convincing image. The disconnect between the simulated and experimental *U-curves* indicates that the model does not represent the physical system accurately. The mismatch is likely due to a combination of modelling errors and wayward hardware operation; particularly the ineffective isolation of current to the active electrode pair.

4.3 Network performance

This Section demonstrates that the ANNs trained on simulated data are capable of performing the EIT inverse problem.

The network's ability to generalise and its robustness to noise are investigated. This involves reconstructing shapes that the networks have not been exposed to, as well as reconstructing multiple objects. The networks have all been trained on 50 000 examples of a randomly sized and placed single circular inhomogeneity, as described in Section 3.5.3.

To test the reconstruction, a newly created randomised inhomogeneity is constructed and the forward problem is solved to obtain the resulting boundary voltages. The inhomogeneous signal is corrupted before calculating the difference signal for the networks' input. The signals are corrupted with 20 dB and 5 dB SNR for the generalisability and robustness tests respectively.

The corrupted inhomogeneity is also used to calculate inverse problem classically for comparative purposes. This is done using the *Gauss-Newton* one-step solver and a Tikhonov

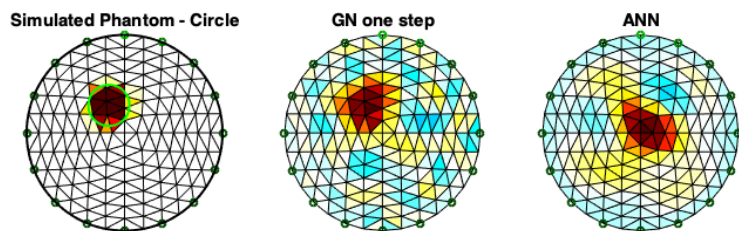
image prior with a regularisation factor of 3E-3 for E16 and 3E-6 for E32.⁶

4.3.1 16-Electrode Model

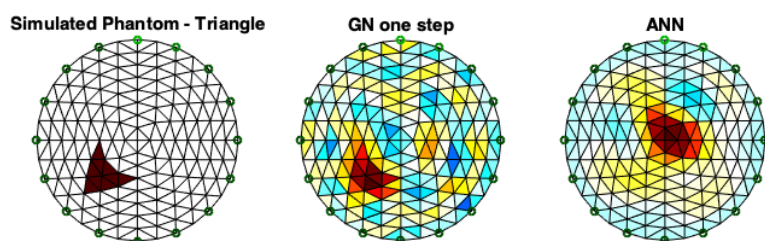
ANN Reconstruction

The trained ANN is not capable of performing the EIT reconstruction. The network shows no ability to generalise and has severely overfitted to the training data. The network appears to have learned a single output which minimises the loss across the entire training set. Effectively, the network illustrates where the training data is most likely to occur. The noise rejection capabilities of the network are therefore not investigated.

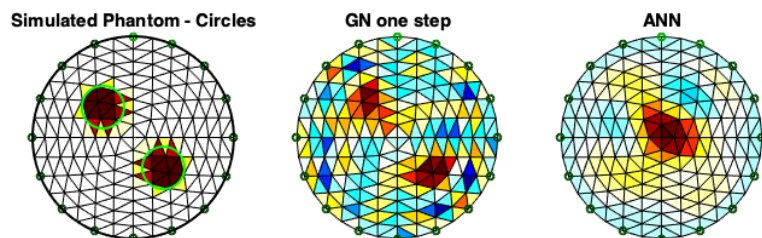
⁶The smaller regularisation factor on the E32 model is required for the inverse solution to converge comparably to the E16 model's solution.



(a) Reconstruction of a circular inhomogeneity (simulated location in green). 20 dB SNR.



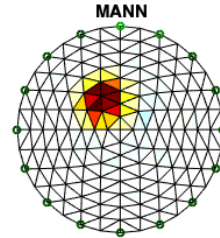
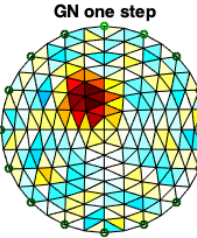
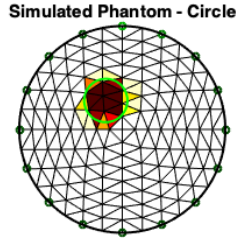
(b) Reconstruction of a triangular inhomogeneity



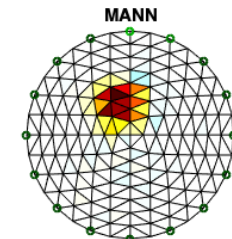
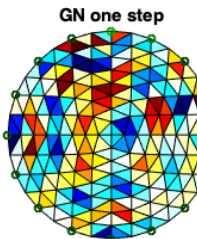
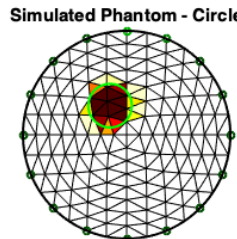
(c) Reconstruction of two circular inhomogeneities (simulated locations in green).

Figure 34: E16 ANN robustness tests as compared to the GN one step.

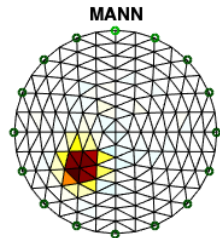
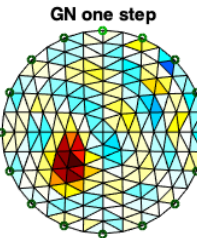
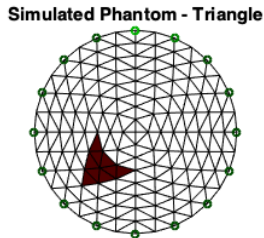
MANN Reconstruction



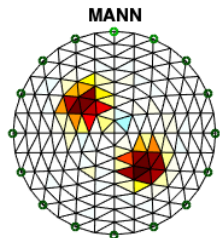
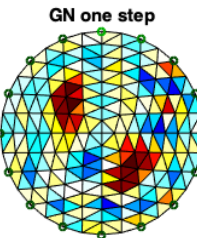
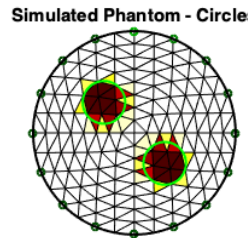
(a) Reconstruction of a circular inhomogeneity (simulated location in green). 20 dB SNR.



(b) Reconstruction of a circular inhomogeneity. 5 dB SNR



(c) Reconstruction of a triangular inhomogeneity



(d) Reconstruction of two circular inhomogeneities.

Figure 35: E16 MANN robustness tests as compared to the GN one step.

Figure 35a shows that the E16 MANN is indeed capable of solving the inverse problem. The network has learned to filter the noise from the input signal (35b) and reconstructs

a much cleaner image than the GN method. Additionally, the MANN’s reconstruction appears to have a smaller size error than the GN method.

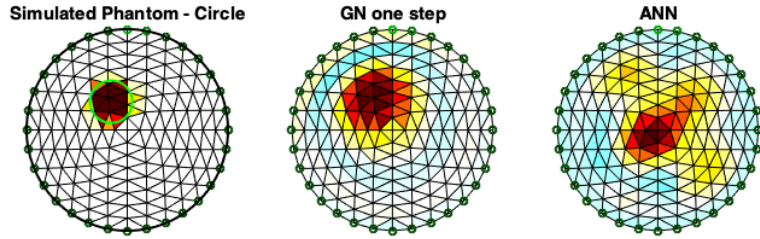
The network robustness is demonstrated in Figure 35c, where an unknown inhomogeneous shape has been introduced. Of the two reconstructions, the GN interpretation of the triangular shape is more accurate in shape than the MANN’s diamond-shaped reconstruction. This shows that the network is less sensitive to the changes in conductivity furthest from the electrodes. Despite being trained on $\{\sigma_{sim}\}$, the networks responsible for the central elements seem to have learned the inherent insensitivity associated with the adjacent stimulation pattern.

Figure 35d shows that the MANN can reconstruct multiple distinct objects despite being trained exclusively on data with a single object. The individual networks of the MANN are therefore sensitive to distinct parts of the output signal.

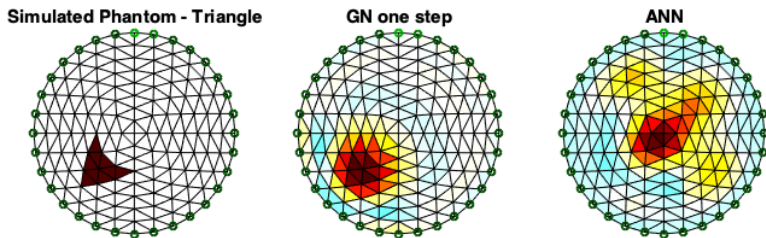
4.3.2 32-Electrode Model

ANN Reconstruction

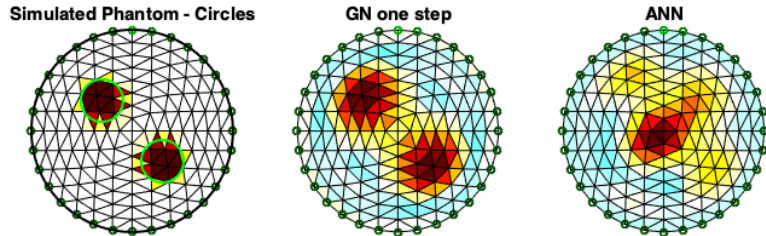
Here too, the network has not learned to generalise and the training data has been severely overfit. Consequently, the network’s ability to reject noise is not investigated.



(a) Reconstruction of a circular inhomogeneity (simulated location in green). 20 dB SNR.



(b) Reconstruction of a triangular inhomogeneity



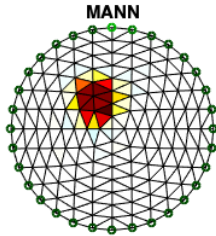
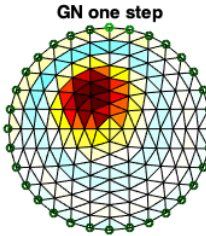
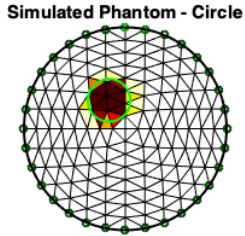
(c) Reconstruction of two circular inhomogeneities.

Figure 36: E32 ANN robustness tests as compared to the GN one step.

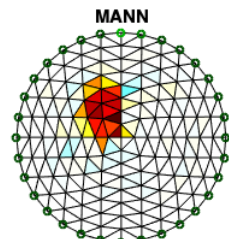
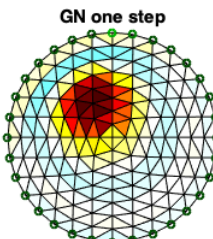
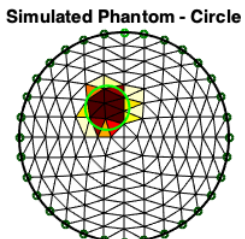
MANN Reconstruction

As with the E16 MANN, the E32 MANN is similarly capable of solving the inverse problem. The MANN reconstruction is visually more accurate than the GN reconstruction of the E32 model and similarly has learned to filter the noise from the input data.

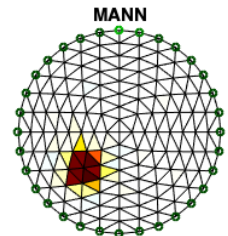
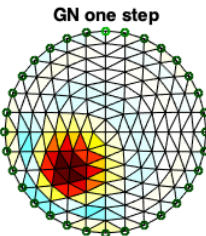
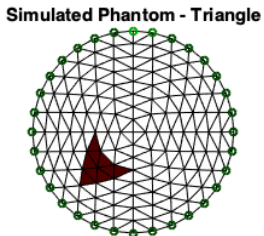
The additional spacing between electrodes in the E32 model has a significant impact on the GN reconstruction quality. However, this additional non-linear characteristic of the input data has been adopted by the MANN.



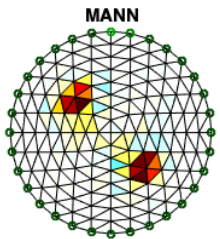
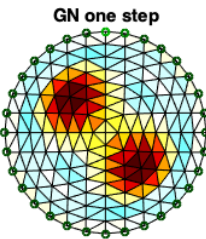
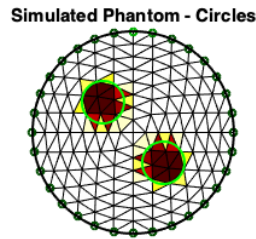
(a) Reconstruction of a circular inhomogeneity (simulated location in green).



(b) Reconstruction of a circular inhomogeneity. 5 dB SNR



(c) Reconstruction of a triangular inhomogeneity



(d) Reconstruction of two circular inhomogeneities (simulated locations in green).

Figure 37: E32 MANN robustness tests as compared to the GN one step.

Again, similarly to the E16 model, the MANN has poor sensitivity near the tank centre as the triangular reconstruction in 37c is similarly diamond-shaped.

Finally, the E32 MANN demonstrates the localised sensitivity of each element's ANN, as

it is also able to reconstruct two distinct objects.

5 RESULTS

This Section compares the reconstruction performance of each network. Since the ANN models are not suitable for the reconstruction task, they are not considered.

The performance of each network first measured using simulated data. The networks are then evaluated on their reconstruction of the measured data.

5.1 Network Performance - Simulated data

The network input data is obtained by solving the forward problem on a randomly placed and sized circular inhomogeneity. The recorded results are the averaged scores obtained over fifty trials. The networks are compared against the GN one-step inverse solver with a Tikhonov prior and a regularisation parameter of 3E-3 and 3E-6 for the E16 and E32 models respectively. The network reconstruction quality is quantified using the following metrics:

Mean Squared Error (MSE): A measure of the network's overall accuracy. An MSE near zero indicates a well-learned task. In this case, only $L(L - 1)/2 = 120$ of the measurements are independent. Therefore solving for $N = 256$ outputs is under-defined. As a result, the MSE of the system cannot be expected to reach zero.

$$MSE = \frac{1}{256} \sum_{i=1}^{256} [\sigma_{sim}(i) - \sigma_{net}(i)]^2 \quad (22)$$

Where $\sigma_{sim}(i)$ is the i th element in the simulated set of conductivities and likewise for the network output, $\sigma_{net}(i)$.

Correlation Coefficient (R): A normalised measure of similarity between the outputs. A value of 1 indicates perfect correlation, whereas 0 indicates no correlation.

$$R = \frac{\sum_{i=1}^{256} (\sigma_{sim}(i) - \bar{\sigma}_{sim})(\sigma_{net}(i) - \bar{\sigma}_{net})}{\sqrt{\left[\sum_{i=1}^{256} (\sigma_{sim}(i) - \bar{\sigma}_{sim})^2 \right] \left[\sum_{i=1}^{256} (\sigma_{sim}(i) - \bar{\sigma}_{sim})^2 \right]}} \quad (23)$$

Percentage Size Error (PSE): A comparison of the reconstructed object's size with respect to its actual size. The PSE is calculated by counting the number of elements

above a threshold conductivity value, σ_{thresh} , where $\sigma_{thresh} = 0.8 \max(\sigma_{sim})$.

$$PSE = \frac{\sum_{256}(\sigma_{net} \geq \sigma_{thresh})}{\sum_{256}(\sigma_{sim} \geq \sigma_{thresh})}\% \quad (24)$$

Table 4 summarises the testing results and highlights the **best** and **worst** reconstruction tools according to each metric.

For both models, reconstruction through computational intelligence leads to a higher quality image. The MANNs achieve a reconstruction that is two and three orders of magnitude greater than their accompanying classical methods. The significant improvement in reconstruction quality is not only a testament to the ANN's ability to filter noise, but also to the ANN's ability to learn complex non-linear functions.

However, the poor \overline{MSE} achieved by the GN reconstructions is not necessarily an indication of a poor reconstruction. The GN method is very effective at *detecting* and *locating* the inhomogeneity. The estimated $\{\sigma\}$ is then iteratively tuned until the solution converges. In this case, the solution is extracted after a single iteration.

Table 4: MANN performance evaluation

	20 dB SNR				5 dB SNR			
	E32 Model		E16 Model		E32 Model		E16 Model	
	GN	MANN	GN	MANN	GN	MANN	GN	MANN
\overline{MSE}	1.0807	0.0184	1.2434	0.0017	1.1417	0.1192	1.2434	0.0222
\overline{R}	0.8288	0.9218	0.4695	0.9625	0.5043	0.5754	0.1404	0.8348
\overline{PSE}	200.6%	71.82%	253.2%	132.2%	240.3%	47.98%	290.6%	110.9%
$\overline{t_{reconstr}}$	0.08	2.49	0.09	2.29	0.10	2.68	0.14	2.45

The high \overline{R} achieved by the E32 GN reconstruction proves the method's effective location and detection ability. The E16 GN method's consistently substandard performance is surprising, considering the comparatively good performance of the E32 GN model. This discrepancy can be attributed to the different regularisation parameters assigned to each model. If a smaller regularisation parameter were applied to the E16 model, its reconstruction quality would improve.

The iterative numerical methods are particularly suited to problems with small changes in the conductivity distribution. However, in these simulations, there is a 100% conductivity difference between the object and background. Consequently, the GN methods tend to soften the sharp conductivity transitions causing a blurring effect. This increases the apparent size of the reconstructed object, with the GN methods overestimating the object size twofold.

The MANNs provide much closer estimates of the object size. The E32 MANN has, on average, the best estimate of object size and is the only reconstruction method to *underestimate* the object size.

The GN methods are at least, significantly faster than the networks. However, solving the inverse problem for the networks requires the input signal to be fed through 256 separate ANNs. Since the network outputs are independent, the reconstruction time can be significantly improved through parallel processing.

Naturally, the reconstruction quality is impaired throughout with a reduction in SNR, but even under these conditions, the MANN remains significantly more accurate than the classical method. The E16 MANN demonstrates a much higher ability to reject noise than any other reconstruction method.

Based on these results, one would expect that the E16 MANN is best suited to solving the reconstruction problem for the measurement data.

5.2 *Network Performance - Measured data*

The networks are applied to the measured data set and compared against the GN one step reconstruction. The difference between the measured homogeneous and inhomogeneous sets is calculated and fed to the networks.

In Figure 38, neither the classical, nor the MANN reconstructions resemble tank. The reconstructions are both unintelligible and give no indication as to the potential size or location of the banana. The MANN reconstruction has interpreted many localised conductivities with a very low conductivity estimation near the tank centre. These point like elements may be the artefacts of noise in the measurement set. The input signal obtained from the measurement data (Figure 32b) shows a markedly less distinct difference than the simulated inputs on which the network was trained. The network expects an inhomogeneity to be represented by a sharp and small, trident shaped signal. However, the measurement set produces an array of jagged edges which are orders of magnitude larger than the simulated inputs. Although the MANNs demonstrated the ability to reject up to 5 dB SNR noise level, the combination of an unfamiliar signal shape and lack of distinction makes the measurement data untranslatable by the network.

There is little visual correlation between the reconstructed classical and network images. However, because the networks were not trained to give the same outputs as the classical methods, these outputs are not expected to be well correlated. The averaged correlation coefficient calculated between the E16 reconstructions is 0.043 and 0.1419 for the E32 model. These are extremely low and indicate that the measurements led to no common emergent interpretation.

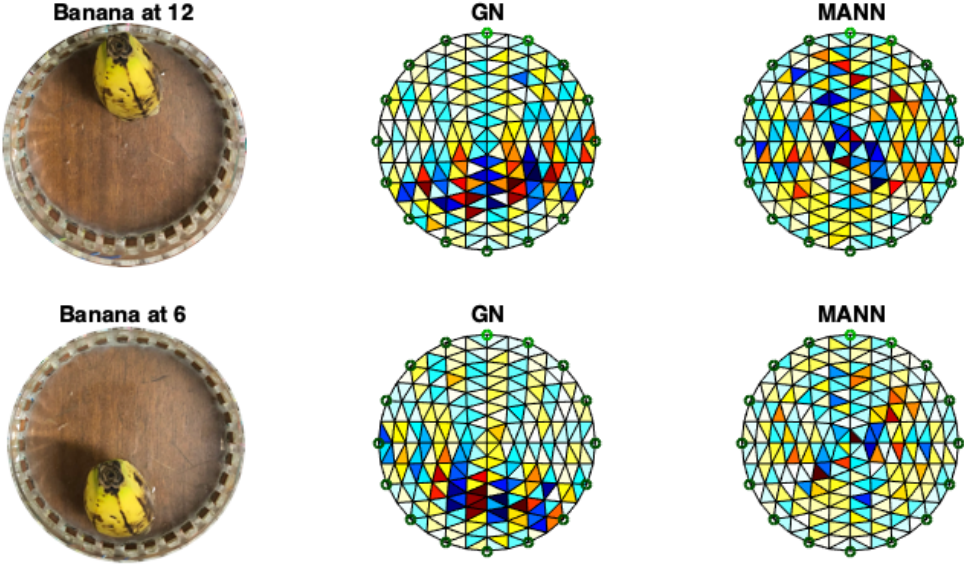


Figure 38: E16 model MANN reconstruction of the experimental measurements for a banana placed in the tank at 6 and 12 o’clock.

6 DISCUSSION

The EIT system, made from several functional, or partially functional, units has failed to integrate the various subsystems. This Section expounds on the fortuitous design decisions and explores the system’s short-comings.

6.1 Hardware Performance

The EIT system has a stable current-source that remains within $\pm 5\%$ of the design value over a significant load impedance. The system was also shown to be stable for a range of frequency values. As the signal source, this is a logical starting point to scrutinise.

Although the current stability experiments show an ostensibly stable signal source, these experiments were restricted to purely resistive loads. Therefore, the stability of the current source comes into question when driving a conductive load through a set of electrodes and non-ideal multiplexers.

The electrodes potentially introduce another source of error to the system. The measured resistance of the tank electrodes ranged between 0.2 and 0.8 Ω , but the contact impedance was not measured, and nor did the EIDORS simulations consider electrode

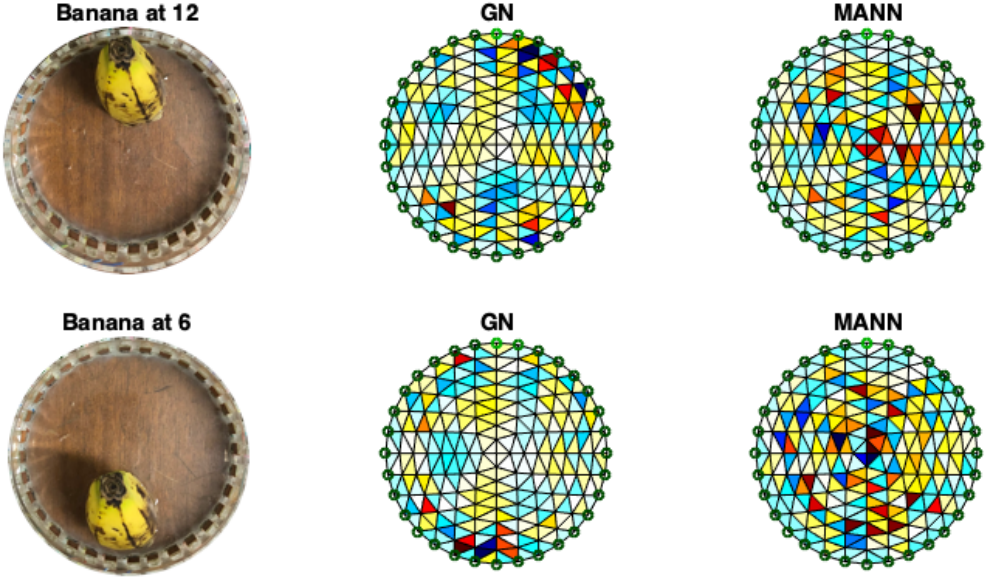


Figure 39: E32 model MANN reconstruction of the experimental measurements for a banana placed in the tank at 6 and 12 o’clock.

contact impedance.

The multiplexers introduce the most uncertainty to the design. The inability of the multiplexers to isolate the current-signal to the active electrode pair has serious detrimental effects on the measurement set. This can be seen in the *U-curves* obtained from a measurement set taken through the multiplexers. Current at the active pair’s neighbouring electrodes is likely causing the uncharacteristic profile where double the number of expected *U-curves* are found. A set of measurements obtained without the multiplexer confirm this.

Unfortunately, the multiplexing was not the undoing of this system as no intelligible image could be constructed from a measurement set recorded without multiplexing.

6.2 EIDORS models

The hardware system is expected to perform reliably but mostly, it must be predictable. For the model to predict the hardware behaviour it must be assiduously configured. Here, two models are created to represent the physical system, one with 16 electrodes and another with 32. The foremost difference being, the slight modification of the stimulation and measurement pattern to account for the interleaving of current injecting, and voltage

measuring electrodes on the E32 model.

Practically, the MANN modelled on the 16 electrode model produced the highest quality reconstruction. However, the measurement set profile for the E32 system is a closer match to the recorded measurement set.

The main discrepancies in the modelling process then include (but are not limited to), input signal modelling, electrode contact impedance and accurate SNRs on the input data.

The input signal in the system is a sinusoidal time-varying signal at a single frequency, whereas the EIDORS model's undergo a frequency domain simulation at all frequencies with a constant amplitude of 1 mA. Therefore, the behaviour of the model is expected to diverge somewhat from reality.

Finally, the models both ignore the discrete and distinct contact impedances of the electrodes. This may not prove to be an insignificant non-linearity.

6.3 Network Performance

The effectiveness of the ANN's could not be determined as they were stubbornly overfitted. This occurred despite implementing various measures to prevent overfitting such as early stopping and validation sets. However, the MANNs trained using the Levenberg-Marquardt algorithm proved to be very effective at performing the EIT inverse problem. The MANNs demonstrated the ability to reject noise in the input signal and produced much higher quality images than the classical method.

The multiplicity of the network architecture requires less of the problem to be defined for each unit. Therefore, the task of learning to generalise a single output based on the entire measurement set becomes much simpler. Additionally, this means that the network training time is reduced, the network accuracy improves, and the network's non-linear representative capacity grows.

6.4 Network Transferal

The MANNs are capable of some degree of generalisability; whereby the networks can reconstruct an image containing multiple objects when never having explicitly learned to do so. This has also been shown for shapes foreign to the network.

Unfortunately, the networks were not transferable to the experimental measurements. Although, it must be noted that this is more than likely attributable to the poor measurements obtained from the hardware system, and the transferability of the networks cannot be de-

duced from the results in this paper.

7 RECOMMENDATIONS

The approach to solving many of the problems encountered in this paper follow the preinciples of Occam's Razor - favouring the simplest solution. This approach is a product of time, resource and knowledge limitations. There are many potential areas of improvement which could lead to a functional system that blends hardware and computational intelligence.

The main points of improvement are listed as:

Hardware Improvements

- Signal Multiplexing: The efficiency, compactness and cost effectiveness of the single source system make it the more appealing implementation for this type of project. However, the non-idealities of the multiplexer must be accounted for. This may be achieved through acquisition of a specialised IC analogue multiplexer, such as the ADG506AKN or through the addition of some selectively active circuit element at the multiplexer outputs.
- ADC Preconditioning: To minimise the noise seen at the output of the system, fourth-order band-pass Butterworth filter are recommended to fastidiously remove any frequency not related to the input signal. An improvement in the SNR will in turn improve the reconstruction quality.
- Adaptation of the measurement system and GUI to allow for continuous image reconstruction. Such a program would allow for rapid prototyping on an interactive system as opposed to testing at subsystem level.

System Modelling

- To accurately characterise the system's boundary voltage development and interaction with the current streamlines, the current must be modelled as a time varying signal.
- The contact impedance on the electrodes should also be characterised and replicated in simulation to maximise the correlation between simulation and reality.

Machine Learning

The multiple ANNs proved to be an effective reconstruction tool. However the ANNs failed to train effectively as they experienced significant overfitting. Future attempts at training are recommended to include dropout. This removes neurones in the hidden layer preventing the network from moulding to the training data. A larger validation set is also recommended.

The quality of the training data is one of the key requirements to learn a task. For this reason, the simulated data is recommended to conform as closely as possible to

the experimental system to facilitate a smooth transferal. This involves introducing an appropriate amount of bandlimited noise to the system.

The simulated inhomogeneities in this paper were all of a uniform conductivity. In the pursuit of network generalisability, it is recommended that future works include variable conductivities to their training examples.

8 CONCLUSION

This paper has presented a simple time-division multiplexed EIT hardware system design (**FS5**). The design's current source is shown to be stable within an accept an accepted tolerance of $\pm 5\%$ for the the range of expected design parameters (**FS0** and **FS1**). Analysis of the signal multiplexing system reveals a lack of signal isolation on the multiplexer output channels. This causes a non-characteristic EIT measurement profile and also contributes to a non-uniform SNR on each of the output channels. This makes the measurement data unsuitable for the EIT problem, despite the system showing sensitivity to conductivity changes at the boundary.

Additionally, the paper has presented two model representations of the physical EIT system. One 16 electrode adjacent-drive adjacent-measurement model which measures all electrodes and a 32 electrode model which models the interleaved current injecting and voltage measuring electrodes with an adjacent-drive pattern on the odd electrodes and an adjacent-measurement pattern on the even electrodes. The 32 electrode model's homogeneous measurement profile is a better representation of the homogeneous measurement profile obtained experimentally (**FS2**).

To perform the reconstruction, this paper presents a shallow ANN and another amalgamation of multiple shallow ANNs. The ANN is overfitted and does not produce any intelligible results, whereas the MANN proves to be a very effective tool for solving the EIT inverse problem. The MANN is robust to noise and maintains a high reconstruction accuracy even when the input signal integrity is reduced to 5 dB SNR. On average, the MANN trained on the 16 electrode model has the highest noise rejection capability as well as accuracy. The MANNs are the slowest inverse solvers with the fast one (E16 MANN) taking 2.29 s. This implies a possible frame rate of (5.12 s per measurement set + 2.29 s per reconstruction) = 7.41 s per frame, partially fulfilling **FS3**.

The networks are applied to the experimental data but are unable to produce any intelligible reconstruction. This is caused by the poor measurement set quality and the subsequently large discrepancy between the input data obtained in simulation and experimentally. Ultimately, the transferability of a network trained on simulated data to an experimental system cannot be measured using this paper. However, a set of recommendations

is made for future work in the area.

REFERENCES

- [1] D. Holder, Ed., *Electrical Impedance Tomography Methods, History and Applications*. Institute of Physics Publishing, 2005.
- [2] A. Miller, B. Blott, and T. Hammes, “Review of neural network applications in medical imaging and signal processing,” *Medical and Biological Engineering and Computing*, September 1992.
- [3] R. AVILL, Y. F. MANGNALL, N. C. BIRD, B. H. BROWN, D. C. BARBER, A. D. SEAGAR, A. G. JOHNSON, and N. W. READ, “Applied potential tomography: a new non invasive technique for measuring gastric emptying,” *Gastroenterology*, 1987.
- [4] B. H. BROWN and A. D. SEAGAR, “The sheffield data collection system,” *Clin. Phys Physiol. Meas.*, vol. 8, no. 91, 1987.
- [5] Y. Zhang and C. Harrison, “Tomo: Wearable, low-cost, electrical impedance tomography for hand gesture recognition,” *Carnegie Mellon University*, 2015.
- [6] W. R. B. Lionheart, “EIT reconstruction algorithms: pitfalls, challenges and recent developments,” *Physiological Measurement*, vol. 25, no. 1, pp. 125–142, feb 2004. [Online]. Available: <https://doi.org/10.1088%2F0967-3334%2F25%2F1%2F021>
- [7] M. Khalighi, B. Vosoughi-Vahdat, M. Mortazavi, and M. M, “Design and implementation of precise hardware for electrical impedance tomography (eit),” *IJST, Transaction of Electrical Engineering*, vol. 38, no. E1, pp. 1–20, 2014.
- [8] M. Soleimani, “Electrical impedance tomography system: an open access circuit design,” *BioMedical Engineering OnLine*, vol. 5, no. 1, p. 28, 2006. [Online]. Available: <http://dx.doi.org/10.1186/1475-925X-5-28>
- [9] V. Cherepenin, A. Karpov, A. Korjenevsky, V. Kornienko, Y. Kultiasov, A. Mazaletskaya, and D. Mazourov, “Preliminary static EIT images of the thorax in health and disease,” *Physiological Measurement*, vol. 23, no. 1, pp. 33–41, dec 2001. [Online]. Available: <https://doi.org/10.1088%2F0967-3334%2F23%2F1%2F304>
- [10] R. W. M. Smith, I. L. Freeston, and B. H. Brown, “A real-time electrical impedance tomography system for clinical use-design and preliminary results,” *IEEE Transactions on Biomedical Engineering*, vol. 42, no. 2, pp. 133–140, Feb 1995.
- [11] D. Murphy and P. Rolfe, “Aspects of instrumentation design for impedance imaging,” *Clinical Physics and Physiological Measurement*, vol. 9, no. 4A, pp. 5–14, nov 1988. [Online]. Available: <https://doi.org/10.1088%2F0143-0815%2F9%2F4a%2F002>
- [12] R. Pallás-Areny and J. Webster, *Analog signal processing*, ser. A Wiley interscience publication. Wiley, 1999.
- [13] J. Webster, *Electrical Impedance Tomography*, ser. Biomedical Engineering Series. Adam Hilger, 1990.
- [14] K. F. Warnick, *Numerical methods for engineering*. SciTech Pub., 2011.
- [15] N. Paleker, “Implementation of data capturing, data processing and an iterative reconstruction algorithm for electrical resistance tomography,” Master’s thesis, University of Cape Town, October 2018, Honor’s thesis.

-
- [16] B. H. Brown, D. C. Barber, and A. D. Seagar, “Applied potential tomography: possible clinical applications,” *Clinical Physics and Physiological Measurement*, vol. 6, no. 2, pp. 109–121, may 1985. [Online]. Available: <https://doi.org/10.1088%2F0143-0815%2F6%2F2%2F002>
 - [17] T. M. Mitchel, *Machine Learning*. McGraw-Hill, 1997.
 - [18] A. Adler and R. Guardo, “A neural network image reconstruction technique for electrical impedance tomography,” *IEEE Transactions on Medical Imaging*, vol. 13, no. 4, pp. 594–600, Dec 1994.
 - [19] Chao Wang, Jian Lang, and Hua-Xiang Wang, “Rbf neural network image reconstruction for electrical impedance tomography,” in *Proceedings of 2004 International Conference on Machine Learning and Cybernetics (IEEE Cat. No.04EX826)*, vol. 4, Aug 2004, pp. 2549–2552 vol.4.
 - [20] H.-C. Kim, C.-J. Boo, and M.-J. Kang, “Image reconstruction using genetic algorithm in electrical impedance tomography,” in *Neural Information Processing*, I. King, J. Wang, L.-W. Chan, and D. Wang, Eds. Berlin, Heidelberg: Springer Berlin Heidelberg, 2006, pp. 938–945.
 - [21] R. Crompton, “Electrical impedance tomography (EIT) reconstruction using machine learning,” Honor’s Thesis, October 2018.
 - [22] S. Martin and C. T. M. Choi, “Nonlinear electrical impedance tomography reconstruction using artificial neural networks and particle swarm optimization,” *IEEE Transactions on Magnetics*, vol. 52, no. 3, pp. 1–4, March 2016.
 - [23] T. Rymarczyk, G. Kłosowski, E. Kozłowski, and P. Tchūrzewski, “Comparison of selected machine learning algorithms for industrial electrical tomography,” *Sensors*, vol. 19, no. 7, p. 1521, 2019.
 - [24] Division of Water Quality, California State Water Resources Control Board (SWRCB). Electrical conductivity/salinity fact sheet.
 - [25] M. S. Tšoeu and M. R. Inggs, “Electrical impedance tomography using code division multiplexing,” in *AFRICON 2015*, Sep. 2015, pp. 1–5.
 - [26] M. S. Tšoeu and R. Inggs, “Capabilities of code division multiplexed electrical impedance tomography,” in *2017 IEEE International Conference on Imaging Systems and Techniques (IST)*, Oct 2017, pp. 1–6.
 - [27] A. Adler and W. R. B. Lionheart, “Uses and abuses of eidors: an extensible software base for eit,” *Physiological Measurement*, vol. 27, no. 5, pp. S25–S42, 2006.
 - [28] S. Ioffe and C. Szegedy, “Batch normalization: Accelerating deep network training by reducing internal covariate shift,” *CoRR*, vol. abs/1502.03167, 2015. [Online]. Available: <http://arxiv.org/abs/1502.03167>

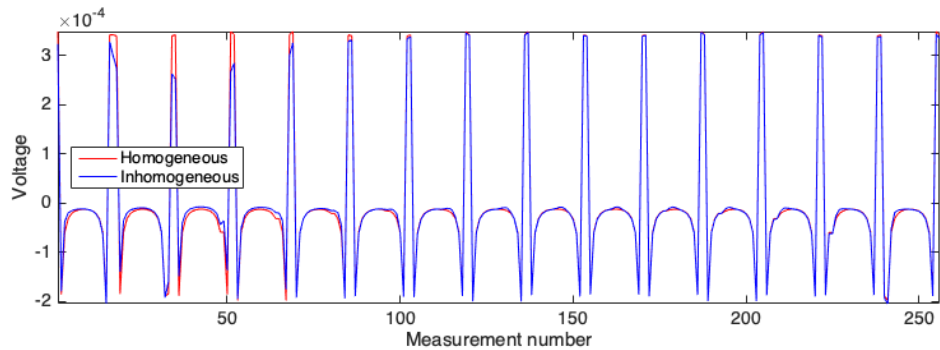
APPENDIX

A GITHUB REPOSITORY

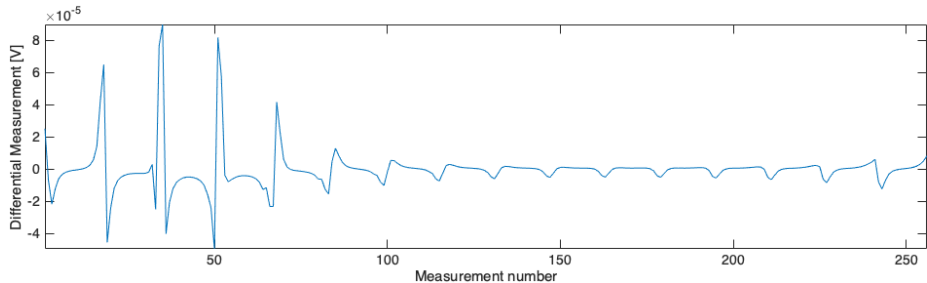
All relevant scripts and data files can be found in the paper's associated online repository [here](#).

B E32 MODEL INPUT DATA FORMAT

The E32 model is used to generate a set of boundary voltages for the homogeneous and inhomogeneous sets of data. This measurement profile matches the experimental results more closely than the E16 model. The results are shown in the Figure B.1.



(a) Homogeneous and inhomogeneous boundary measurements obtained from the E32 EIDORS model.



(b) Difference between the homogeneous and inhomogeneous boundary measurements.

Figure B.1: ML algorithm input data profile for the E32 model.